Juuso Terävä

Simulating Helium Ash in ITER

School of Science

Thesis submitted for examination for the degree of Master of Science in Technology.

Espoo 3.11.2016

Thesis supervisor:

Prof. Mathias Groth

Thesis advisor:

M.Sc. (Tech.) Konsta Särkimäki

AALTO-YLIOPISTO
PERUSTIETEIDEN KORKEAKOULU

DIPLOMITYÖN
TIIVISTELMÄ

Tekijä: Juuso Terävä

Työn nimi: Helium-tuhkan simuloiminen ITER:ssä

Päivämäärä: 3.11.2016 Kieli: Englanti Sivumäärä: 4+46

Teknillisen fysiikan laitos

Professuuri: Plasmafysiikka Koodi: SCI3056

Valvoja: Prof. Mathias Groth

Ohjaaja: DI Konsta Särkimäki

Fuusioplasmoissa syntyy energeettisten alfa-hiukkasten jäähtymisen seurauksena niin sanottua helium-tuhkaa. Tämä helium-tuhka säteilee pois plasman energiaa ja rajoittaa saatavaa fuusiotehoa. Näistä syistä on tulevan ITER-testireakrorin onnistuneen toiminnan kannalta tärkeää, että helium-tuhka saadaan tehokkaasti poistettua koossapidetystä plasmasta. Jotta heliumin määrä reaktorissa pysyy riittävän alhaisena, on myös ehkäistävä koossapidetystä plasmasta jo poistuneen heliumin paluu sinne.

Tässä työssä tutkittiin, voidaanko helium-tuhkan paluuta reaktorin seinältä koossapidettyyn plasmaan ehkäistä luomalla plasman reunalle magneettisia saaria ulkoisten magneettisten häiriöiden (MP:den) avulla. Työssä myös esitellään helium-tuhkan haittavaikutuksia ja aiempia helium-kokeita. Tutkitun menetelmän lisäksi työssä esitellään kaksi menetelmää heliumin poistamiseksi.

Helium-tuhkaa tutkittiin simulaatioilla. Nämä simulaatiot toteutettiin Monte Carlo radanseurantakoodilla ASCOT. ASCOT-simulaatioita on aiemmin tehty lähinnä nopeille ioneille ja onnistuneiden simulaatioiden takaamiseksi termiselle heliumille ASCOT:n numeerinen integraattori päivitettii Euler-Maryuama -menetelmästä Milsteinin menetelmään. Koodiin myös lisättiin uusi adaptiivinen aika-askellus stokastiselle integroinnille.

Simulaatiot tehtiin ITER:n perusplasmalle ja havaittiin, että magneettiset saaret ehkäisevät heliumin palautumista koossapidettyyn plasmaan vain hyvin heikosti. Lisäksi MP:t huononsivat deuteriumin ja alfa-hiukkasten koossapitoa enemmän kuin heliumin.

Avainsanat: Fuusio, Plasmafysiikka, ITER, Tokamak

AALTO UNIVERSITY
SCHOOL OF SCIENCE

ABSTRACT OF THE
MASTER'S THESIS

Author: Juuso Terävä

Title: Simulating Helium Ash in ITER

Date: 3.11.2016 Language: English Number of pages: 4+46

Department of Applied Physics

Professorship: Plasma Physics Code: SCI3056

Supervisor: Prof. Mathias Groth

Advisor: M.Sc. (Tech.) Konsta Särkimäki

As energetic alpha particles cool down in fusion plasmas, they become helium ash. This helium ash radiates away energy from the plasma, dilutes the deuterium-tritium fuel mix and, thus, decreases the achievable fusion power. Therefore, its efficient removal from the confined plasma is essential for successful operation of the future fusion test reactor ITER. It is also important to prevent the return of the helium back to the confined plasma after is has been first removed from there.

In this thesis, simulations were made to examine whether magnetic islands, created by external magnetic perturbations (MPs) due to ELM control coils (ECCs), can be used as a transport barrier to prevent helium from the first wall and divertor from returning to the confined plasma. The issue of helium ash as well as past helium experiments are also reviewed in this work. Along the simulated method, two schemes to improve helium ash removal are also presented in this work.

The simulations were carried out with the orbit-following Monte Carlo code ASCOT. Earlier ASCOT-simulations were done mainly for fast ions, so in order to correctly simulate thermal helium ash, ASCOT's numerical integration scheme for stochastic differential equations (SDEs) was updated from the Euler-Maryuama method to the Milstein method. An adaptive time-stepping scheme for stochastic integration was added to the code.

The simulations were done for the ITER baseline scenario and showed that the transport barrier effect of the islands was weak. The MPs furthermore enhanced the losses of deuterium and alpha particles more than the losses of helium.

Keywords: Fusion, Plasma Physics, ITER, Tokamak

Contents

1 Introduction

Nuclear fusion is a process in which two atomic nuclei merge to form a heavier nucleus. For elements lighter than iron, this process releases energy, and mankind has been determined to master this form of energy production ever since its discovery in the 1930s. The highest energy gains for the process are obtained from light nuclei and, therefore, the isotopes of hydrogen are the chosen fuel for artificial fusion. For a future reactor, an energy gain greater than one, *i.e.* more energy is extracted from the fusion reactions than has been put in to achieve the fusion in the first place, is achieved at lowest temperatures for the fusion of deuterium and tritium. The desired reaction encompasses the formation of one helium nucleus and one neutron from one deuterium and one tritium nucleus:

$$\mathrm{D} + \mathrm{T} \rightarrow {}^4\mathrm{He}(3.5\mathrm{MeV}) + \mathrm{n}(14.1\mathrm{MeV}). \tag{1}$$

The high temperatures of over hundred million kelvins required for the energy gain of over one cause the fusion fuel to be in a plasma state. In plasmas, also called the fourth state of matter, electrons in atoms have overcome the binding energy (about 13.6 eV for hydrogen) due to electromagnetic attraction towards the nucleus, causing atoms to break into their building blocks. In other words, the plasma consists of a kind of gas of free electrons and ions. To obtain fusion output, not only high temperature is required, but the plasma must be confined for a sufficiently long time. The greater-than-one energy gain requires a sufficiently high triple product of energy confinement time τ_E, fusion fuel number density n and temperature T. For DT-fusion, this criterion is [2]

$$n\tau_E T \geq 5 \times 10^{21} \quad \mathrm{m}^{-3}\mathrm{skeV} \tag{2}$$

There are three main ways to obtain high enough triple product: gravitational, inertial and magnetic. The stars are powered by fusion, and the plasma in them is confined by gravity, making gravitational confinement the most common form of confinement in the universe. However, in man-made fusion, the small masses of the fusion fuel involved rule out the gravitational confinement. At any given time, a fusion reactor would contain a maximum of few grams of fuel [1]. In inertial confinement fusion, lasers are used to compress the fuel to make it dense enough to obtain sufficient fusion power. The energy from the fusion is released in a very short period of time. However, the first fusion test reactor ITER, currently being built in France, relies on magnetic confinement. In this form of confinement, magnetic fields are used to confine the electrically charged particles of the plasma via Lorentz force. ITER will be a tokamak reactor, which is an innovation made by Soviet scientists in the 1950s, where a confining magnetic field of a torus-shaped plasma is provided in the toroidal direction (long way around the torus) by magnets and in the poloidal direction (short way around the torus) by inductively driven current [3].

Nuclear fusion offers not only a carbon-free mean to produce energy, but also one that is sustainable even beyond the foreseeable future due to abundant fuel

supply. The deuterium for the process can be found in seawater, a litre of which contains 33 mg of the isotope [1]. Tritium, on the other hand, is radioactive and its half life is only 12 years, making it rare in nature. However, tritium can be bred from lithium, which is found in abundant quantities in Earth's crust, via these reactions:

$$^6\mathrm{Li} + \mathrm{n} \rightarrow {}^4\mathrm{He} + \mathrm{T} \tag{3}$$

$$^7\mathrm{Li} + \mathrm{n} \rightarrow {}^4\mathrm{He} + \mathrm{T} + \mathrm{n}. \tag{4}$$

The tritium for ITER will be provided from global inventory, but ITER's successor DEMO, which will be a full-scale fusion power plant, must obtain its tritium by breeding. The neutrons for the breeding reactions are provided by the fusion reactions, so DEMO still needs tritium for its initial start-up, but would then provide its own tritium [3, p. 21].

Even though the neutrons are required for lithium breeding, their main task is to carry out the fusion power produced in a reactor since they do not interact with the background magnetic field or the plasma. On the other hand, the electrically charged and energetic fusion-born helium nuclei, or fusion alphas, must transfer their energy to the plasma in order to sustain the temperature for more fusion reactions to occur. As the alphas lose their energy, they finally become helium ash. This helium ash radiates energy away from the plasma and dilutes the fuel, reducing fusion efficiency in the process. Therefore, its removal from the plasma is essential for successful operation of any fusion reactor. In this thesis, current status of helium ash removal is explored and new simulations are made to examine some aspects of the removal in ITER.

1.1 Structure of This Thesis

The simulations in this thesis explore the validity of one proposed helium removal mechanism for ITER. The simulated mechanism is motivated experiments in smaller devices and the simulations are done with the orbit-following Monte Carlo code ASCOT [4]. In order to carry out the simulations, some of ASCOT's numerical methods were revised. In chapter 2, the current status of helium ash removal is reviewed. Firstly, the mechanisms through which helium affects the plasma are presented in more detail. Current tokamaks do not produce helium ash. Nevertheless, some experiments with injected helium have been performed to explore the helium removal. Some of these experiments and their results are presented. Three proposed methods to improve helium ash removal, including the one that is simulated, are also introduced.

Chapter 3 describes the mathematics behind the numerical improvements to ASCOT. Essentially, ASCOT solves stochastic differential equations to obtain orbits and distributions for chosen test particles. The new methods improve the numerical integration of these equations to cover particles at thermal energies. To give a thorough presentation of the foundations of these methods, the third chapter

provides basic definitions and concepts from probability theory. A few fundamental definitions and results of Itô calculus, an extension of ordinary calculus to cover stochastic processes, are described. With this background information in place, the new numerical methods are presented. A new scheme to integrate stochastic differential equations in ASCOT, the Milstein method, is derived and its virtues over ASCOT's previous scheme, the Euler-Maruyama method, are discussed. To improve the speed of ASCOT simulations, an adaptive time stepping scheme for integration of stochastic processes is also presented.

Chapter 4 is dedicated to applying the improvements to ASCOT simulations. Firstly, ASCOT's model for particle collisions is presented. Then, an outline is given for the derivation of the stochastic differential equations ASCOT solves to obtain particle trajectories. The application of the numerical methods from chapter 3 to these equations is described and test simulation results are presented, demonstrating that the methods work and that adaptive time-stepping is faster than fixed time-stepping.

Chapter 5 describes the set-up and results of the helium ash simulations. The origin of the background magnetic field of the simulations is briefly described as well as how the simulation test particles were created. A recap of some of earlier ASCOT results is also given. The simulations were done both in the core plasma and at the plasma edge. In the latter case, the helium simulations were compared to similar simulations of deuterium. Chapter 6 gives a summary of this thesis and discussion about the simulation results, including discussion of some of ASCOT's drawbacks as well as ideas for further studies.

2 Helium Ash and its Removal in Tokamaks

Retaining helium ash in the plasma fuel is undesired for two main reasons: it increases radiation losses and dilutes the plasma. The radiation losses arise from the acceleration of charged particles. Because of their lighter mass, the electrons are accelerated significantly more than the ions and are responsible for most of the radiation losses. However, the acceleration of the electrons is increased by the presence of ions with higher charge numbers, such as helium. At these high energies, as expected in ITER, the only relevant radiation mechanism is bremsstrahlung radiation. Bremsstrahlung of radiation arises from acceleration due to particle scattering and is thus present in pure deuterium-tritium plasma as well. The power of bremsstrahlung is proportional to the square of the acceleration a:

$$P = \frac{e^2}{6\pi\epsilon_0 c^3} a^2, \tag{5}$$

where e is the elementary charge, ϵ_0 the permittivity of free space and c the speed of light. The acceleration from collisions arises from the Coulomb force of the interaction between an electron and an ion. This acceleration is

$$a = \frac{Z^2 e^2}{4\pi\epsilon_0 m_e r^2}, \tag{6}$$

where m_e is the mass of electron, r the distance between the electron and the ion and Z is the charge number of the ion. Hence, the total power of bremsstrahlung radiation increases in the presence of helium ash because of its higher charge number [3, p. 228].

The second issue of helium ash is fuel dilution. The electron density of a tokamak plasma has to be kept low enough, to prevent instabilities to occur. The limit on the electron density in turns limits the density of fuel ions because the plasma has to be quasi-neutral, *i.e* $n_e = \sum(Z_i n_i)$. Since the electron density remains constant, accumulation of helium reduces the maximum density that can be achieved by deuterium and tritium [5, p. 20]. The fusion power is proportional to these densities as [3, p. 8]:

$$P = n_D n_T \langle \sigma v \rangle, \tag{7}$$

where n_D and n_T are the deuterium and tritium number densities, respectively, and $\langle \sigma v \rangle$ is the fusion reaction rate. Therefore, helium accumulation reduces the highest achievable fusion power. In turn, conversely, lower power reduces the plasma temperature, which reduces the power even further.

To determine the efficiency of helium removal, it is important to understand what determines the helium confinement time τ_{He}. When determining τ_{He}, two components have to be taken into account: τ_0, the replacement time of helium

from a source in the central plasma, and τ_{edge}, the replacement time for helium from a source on the edge of the plasma. The replacement time refers to the time that helium remains in the region where it is born (central plasma or the edge). Some of the helium from the edge source that exits the confined plasma can still return before it is pumped, among other particles, out of the vacuum vessel using cryopumps. However, the finite efficiency of these pumps (as low as 1 %) allows the majority of helium to return to the confined plasma, via further collisions on the wall, before it is pumped out. Helium is also a noble gas and, therefore, has a very high recycling probability. Combining all these considerations, the formula for the helium confinement time τ_{He} becomes [6]

$$\tau_{He} = \tau_0 + \tau_{edge}\frac{R_{eff}}{1 - R_{eff}}, \tag{8}$$

with

$$R_{eff} = R_{ret} f \frac{1}{1 - (1 - f)R_{ret}}, \tag{9}$$

where R_{eff} is the ratio of helium influx to the confined plasma to the helium outflux from it, R_{ret} is the fraction of helium returning from the first wall and divertor and f is the refuelling efficiency, *i.e.* the efficiency with which the helium returning from the surfaces enters the confined plasma. This re-entry of helium to the confinement is an issue because, inside the confined plasma, helium will move upwards along density gradients, *i.e* towards the core [3, p. 221]. In JET experiments, $R_{eff} > 0.9$ has been observed, although with an error of about 50% [7]. Unfortunately, R_{eff} has not yet been scaled for ITER. What is known is that the fraction of helium ash should be kept below 10% for ITER [3, p. 220]. This corresponds to a low enough ratio $\rho_{WR} = \tau_{He}/\tau_E$ of the helium confinement time τ_{He}, discussed above, and the energy confinement time τ_E [7].

To illustrate the significance of ρ_{WR}, consider a simplified model for a deuterium-tritium plasma first presented in Ref. [6]. In the model, following simplifying assumptions are made: the number densities of deuterium and tritium are equal $n_D = n_T = 0.5n_i$, the plasma contains only one impurity species other than helium ash with charge number Z, the temperature of all plasma components is the same $T = T_e = T_i = T_{He} = T_Z$, fusion alphas transfer their whole initial energy to the plasma, and the pressure of energetic alphas is neglected in the energy balance. It should be noted that especially the assumption concerning the alpha pressure is not valid for ITER [8]. However, the conclusion of the effect of helium on the maximum plasma temperature remains, making the example instructive. Under the given assumptions, the ignition condition, *i.e.* the condition on fusion power that allows the fusion reactions to occur without external heating, for the plasma can be written as

$$\frac{1}{4}n_e^2 f_i^2 E_\alpha \langle \sigma v \rangle = \frac{3}{2}\frac{1}{\tau_E} n_e f_{tot} T, \tag{10}$$

where n_e is the electron density of the plasma, $f_i = n_i/n_e$, $f_{tot} = (n_i + n_z + n_{He)/n_e}$, E_α is the energy of energetic fusion alphas (around 3.5 MeV), and (σv) is the fusion reaction rate. Note that in the ignition condition τ_E contains the radiation losses. Starting from this condition, a solution can be found for $f_{He} = n_{He}/n_e$:

$$f_{He} = \frac{3T[1 - 0.5(Z-1)f_Z]}{\frac{E_\alpha}{\rho_{WR}} + \frac{3}{2}T}, \tag{11}$$

where $f_z = n_Z/n_e$. Equation (11) describes the share of helium in a deuterium-tritium plasma as it ignites. For a deuterium-tritium plasma to ignite, there has to be some deuterium and tritium, *i.e* $f_{He} < 0.5$. This implies an upper bound on the temperature T for which ignition can occur:

$$T < \frac{E_\alpha(1 - Zf_Z)}{(4.5 + 3f_Z - \frac{3}{2}Zf_Z)\rho_{WR}}. \tag{12}$$

The helium density relative to the electron density (f_{He}) therefore limits the temperature for which ignition can occur. This limit establishes a relation between the temperature and the ratio of helium confinement time and energy confinement time (ρ_{WR}). In this relation (12), temperature has an $1/\rho_{WR}$-dependence and, therefore, the maximum temperature the plasma can reach decreases as ρ_{WR} increases, therefore limiting available fusion power. For low levels of impurities, a low enough ρ_{WR} means $\rho_{WR} \leq 10$, but for a carbon concentration of 3%, for example, $\rho_{WR} \leq 5$ is necessary [7].

2.1 Helium Experiments

To understand past experiments of helium, some relevant plasma phenomena present in tokamaks are first described. In the high confinement mode, or H-mode, a transport barrier. The region of the transform barrier is called the pedestal, which manifests itself as a sharp rise in density and temperature at the edge of the plasma, and it allows an improved confinement of the plasma [9]. Low confinement mode, or L-mode, is a mode where the pedestal is not created. Even though H-mode improves the confinement of the plasma, it gives rise to a perturbation called edge localised modes, or ELMs, brief relaxations of the pedestal that deposit large amounts of energy from the pedestal region to the divertor in milliseconds [10]. ELMs can be divided in three main subcategories [3, p. 416]: large type I ELMs causing intolerable heat loads to the wall, intermediate ELMs of type II, and small but continuous type III ELMs contributing to the loss of confinement via their frequency. In addition to the pedestal, there can also be internal transport barriers (ITBs), present deeper in the plasma. The ITBs are created by modifying plasma current profiles and are seen as a path to provide steady-state fusion, *i.e.* fusion without inductive current drive, which will be studied in ITER's advanced operating scenario [11].

Helium confinement has been studied in various tokamaks. A review article by Hogan [12] describes these experiments up to year 1997. Most of these early studies were done in the L-mode, but early ELMy H-mode experiments were done

Table 1: Comparison of ρ_{WR} in DIII-D, JET and JT-60U.

	DIII-D	JT-60U	JET
ELMy H-mode	11	2.8-10	7.2-15
ITB	-	8-10	4-10

in DIII-D [13]. More recent studies have been performed in JET [7] and JT-60U [14] [15]. These studies have been done in ELMy H-mode as well as in the presence of an ITB. Since current tokamaks do not usually produce actual helium ash from cooled down fusion alphas, the ash has been simulated by helium gas injections and helium neutral beam injection (NBI) [7]. In gas injections, helium is injected to the plasma for some finite time, after which no new helium is added. These experiments can be used to analyse helium re-entry. In experiments with the NBI, the injection of new helium is constant throughout the experiment. These experiments can be used to analyse helium transport from the core. Helium NBI is used in the DIII-D experiments [13] and in JET's and JT-60U's ITB experiments [15] [7]. Helium gas puffs were used in the ELMy H-mode experiments of JET and JT-60U [14] [7].

The ρ_{WR} values obtained from the DIII-D, JET and JT-60U experiments are listed in table 1. In the DIII-D and JT-60U experiments, helium removal was limited by the efficiency of the pumping via argon frosting [3, p. 736]. In JT-60U, the ITBs resulted in better helium confinement than ELMy H-mode. In the JET experiments, variation in ρ_{WR} could be explained in terms of differences in the ratio τ_{edge}/τ_E, *i.e.* the ratio of the helium confinement time on the edge to the energy confinement time. These experiments suggested better helium confinement in the ELMy H-mode than with ITBs. Overall, if the impurity content of the plasma is low, implying $\rho_{WR} \leq 10$ is required, the helium removal seems to be sufficient in the presence of ITBs. However, in the ELMy H-mode or in the presence of additional impurities the sufficiency of helium removal is far less certain. Since the impurity mix of ITER is unknown [5, p. 23], additional mechanisms for helium removal have been proposed to ensure smooth operation of ITER.

2.2 Proposed Helium Removal Mechanisms

In this section, three ways to enhance helium removal from ITER are presented. Firstly, sawtooth oscillations can transport helium from the core of the plasma to its edge [16]. Secondly, the ion cyclotron resonance heating, or ICRH, can be used to push the helium from the edge to outside the confined plasma [17]. Lastly, external magnetic perturbations, or MPs, used for ELM mitigation can shape the magnetic field at the edge to reduce helium re-entry [19].

Sawtooth oscillations take their name from the shape of the temperature profiles they cause. In the ramp-up phase of the oscillations, both quantities rise steadily in the core plasma and decrease further out on the edge. After the ramp-up, the temperature and density collapse within about 100 μs to a lower level in the core and correspondingly increase at the edge (Fig 1). The oscillations are usually (but

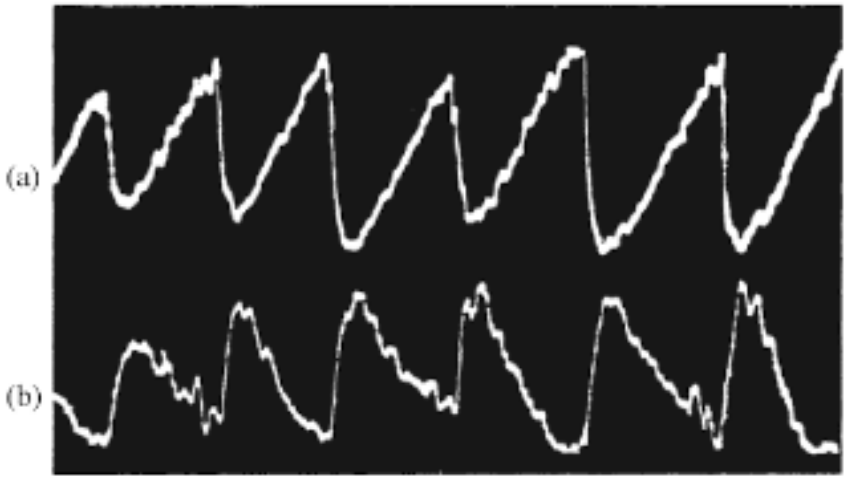

Figure 1: X-ray emission from (a) central and (b) outer plasma during sawtooth oscillations. Image courtesy of Wesson [3, p. 370]

not always) initiated by an MHD instability, arising from a perturbation ϵ in various plasma quantities, such as the magnetic field, of the form $\epsilon \propto \exp(im\theta - in\phi)$, where θ is the poloidal and ϕ the toroidal angle [16]. For the sawtooth-initiating instability, the poloidal (m) and toroidal (n) mode numbers are both equal to one. This kind of instability may only occur in the vicinity of the $q = 1$ magnetic flux surface, where q is the safety factor, *i.e.* the the number of toroidal revolutions of a magnetic field line per one poloidal revolution. In the crash, the inner region of the plasma (where $q < 1$) is displaced and it magnetically reconnects with the outer region (where $q > 1$). The temperature of the inner region drops due to the reconnection, and this $q < 1$ region starts to shrink before disappearing altogether (Fig. 2) [3, p. 369].

For tokamak operation the sawtooth crash is a double-edged sword: depending on its severity, it can either initiate a disruption of the plasma or increase the plasma confinement. During the crash, the temperature remains constant within the inversion radius. In case of an inversion radius of greater than half of the minor radius of the tokamak, and with energy losses of order of keV, the sawtooth crash can lead to ELMs and other severe instabilities leading to disruption. On the other hand, if the inversion radius and the energy losses from the crash are sufficiently small (less 40% of the minor radius and fraction of a keV, respectively), repeated sawtooth oscillations may remove accumulated helium and other impurities from the core plasma. The sawtooth oscillations could be controlled by modifying the current profile of the plasma or by modifying the distribution of fast ions. The latter is especially relevant for ITER, since it will be the first machine to contain significant number of fusion-born alpha particles. The fast ion distribution can be controlled by injecting energetic neutral particles in the plasma (NBIs) or by using ion cyclotron resonance heating (ICRH), where an electromagnetic wave is used to energise plasma ions [16].

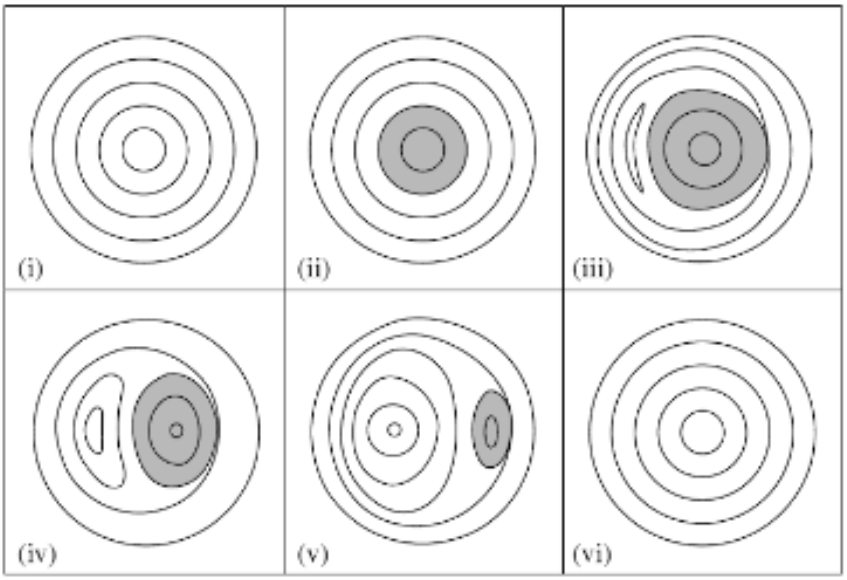

Figure 2: Magnetic flux surface structure during a sawtooth crash. The shaded region represents the $q < 1$ region. Image courtesy of Wesson [3, p. 372].

ICRH plays also a key role in the second proposed method to improve the helium transport from the confined plasma to outside it. In this method, the ICRH wave, with the correct ion cyclotron resonance frequency (ICRF), couples with the helium and accelerate it towards the edge plasma [17]. Applying ICRH to helium ash requires the ash to be partly ionised to He^+ instead of fully ionised He^{2+}. This is because He^{2+} has the same resonant frequency as deuterium, which should be kept confined. However, at electron temperatures higher than 100 eV, which will be the case in ITER, helium is usually in the fully ionised state. Obtaining the He^+ for ion cyclotron heating could be realised via charge exchange with neutral deuteron or tritium, which can be found at the plasma edge. Given that the lifetime and the ionisation mean free path length of He^+, *i.e.* the average length the ion travels before a change in its charge state, are long enough, a wave with the correct resonant frequency could accelerate them perpendicularly to the magnetic field. The pitch of the particle would decrease as the velocity perpendicular to magnetic field increases and the particle would become ripple-trapped. Once trapped, ∇B-drift would transport the helium out of the plasma.

The third proposal to improve helium removal, is to use external magnetic perturbations (MPs), produced by ELM control coils (ECCs) and used to mitigate ELMs. Since the ELMs actually improve impurity transport themselves, any method to mitigate them should keep this desirable effect while getting rid of the negative ones. The MPs achieve that by making the edge of the tokamak's magnetic field stochastic with small perturbations (amplitude of the perturbations was 0.25% of the equilibrium field in case of the first experiments in DIII-D) [18]. Additionally, the MPs can be fine tuned, so in addition to the increase in the field lines stochasticity at the very edge of the plasma, magnetic islands appear further inside (see Fig. 3 for illustration). These islands are the result of a magnetic reconnection of the field lines and could function as an additional transport barrier, which prevents the helium from re-entering the confined plasma after it is first lost. Experiments on this method have been performed in the LHD stellarator and in the TEXTOR tokamak [19]. In TEXTOR, the introduction of the magnetic islands by RMP reduced the decay time of helium gas puffs by a factor of about three. In LHD, the effective confinement time of helium was reduced by about 30% in the presence of magnetic islands. The introduction of magnetic islands also reduced the ratio He/H as detected in the intensity of emission lines in LHD, indicating that the islands have a favorable effect specifically on helium. In this thesis, simulations are made to see whether the LHD and TEXTOR results can potentially be extended to ITER.

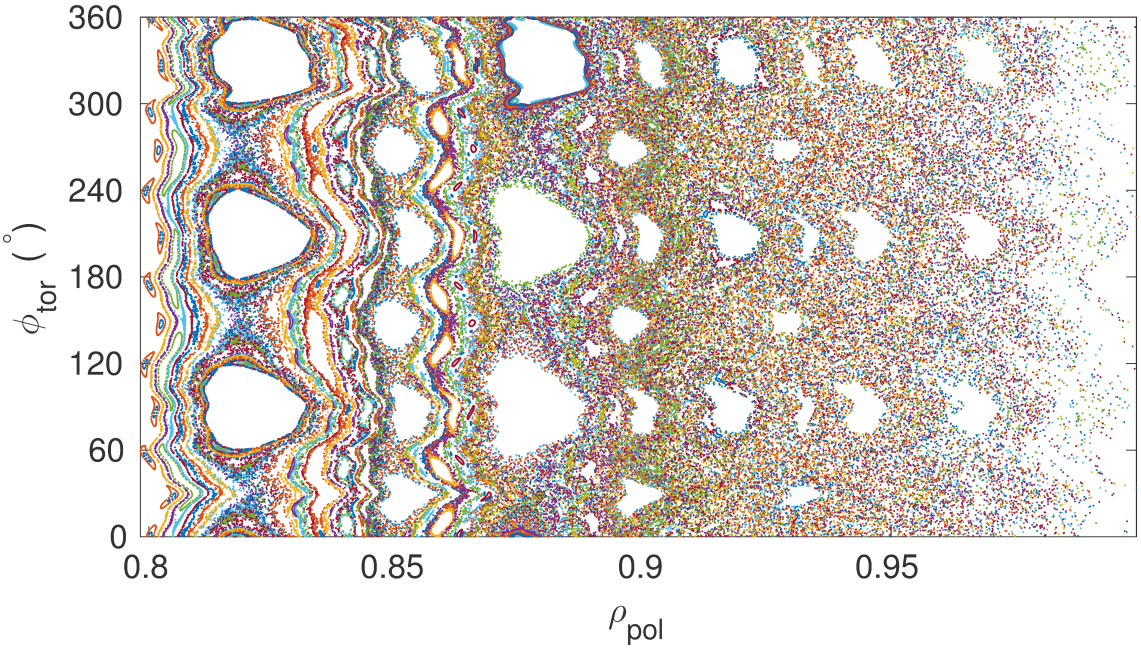

Figure 3: Poincaré plot of magnetic field lines in ITER baseline scenario at outer midplane in the presence of MPs. The MPs have $n = 3$ and the current in the ECCs is 45 kA. ρ_{pol} is the square root of the normalised poloidal magnetic flux. Stochasticity of field lines and island structures are clearly visible. The field lines were initiated at $\phi_{tor} = 0°$ and therefore no magnetic field lines appear inside the magnetic islands. The plot was generated with ASCOT's FILIP module [20, p. 43], and the magnetic background data was obtained from the RIPLOS2 project [21].

3 Numerical Methods for Stochastic Integration

To carry out the helium ash simulations, the orbit-following Monte Carlo code ASCOT [4] was used. ASCOT solves *stochastic differential equations* (SDEs) for particle trajectories and sums individual trajectories to obtain the distribution function of the simulated particles. For the helium ash simulations, the integration of the SDEs in ASCOT was updated with a new integration scheme and adaptive time stepping. To investigate the impact of these numerical changes, review of some definitions from probability theory are necessary as they are required in the derivation of the new methods. For a thorough examination of the following concepts in probability theory and stochastic processes see Ref. [22].

A probability space $(\Omega, \mathcal{F}, P)$ consists of possible outcomes Ω, a set of events $\mathcal{F}$ and probabilities P assigned to each event. For example, when tossing a fair coin once, one has two outcomes: heads (H) or tails (T). An event in $\mathcal{F}$ is a combination of zero or more outcomes. The two outcomes of a fair coin toss have four such combinations: heads $\{H\}$, tails $\{T\}$, nor heads nor tails $\{\}$ and heads or tails $\{H, T\}$. When probabilities are assigned to these events, the first two have probability of half each, the third event has probability zero and the last event has probability one. In a mathematically rigorous definition, the set of events $\mathcal{F}$ has to be a *σ-algebra* of the outcomes Ω, which requires the following:

1. $\emptyset \in \mathcal{F}$, *i.e* empty set belongs to $\mathcal{F}$
2. $\mathcal{E} \in \mathcal{F}$ ($i.e$ $\mathcal{E} \subset \Omega$) $\Rightarrow \mathcal{E}^c \in \mathcal{F}$, where $\mathcal{E}^c$ is the compliment of $\mathcal{E}$ (*i.e.* $\mathcal{E}^c = \Omega \backslash \mathcal{E}$). In other words, for every element $\mathcal{E}$ of $\mathcal{F}$, the compliment of $\mathcal{E}$ must also be an element of $\mathcal{F}$.
3. If K is a countable set, $k \in K$ and $\mathcal{E}_k \in \mathcal{F}$, then $\forall\ k \Rightarrow \bigcup_K \mathcal{E}_k \in \mathcal{F}$. In other words, a countable union of elements of $\mathcal{F}$ must also be an element of $\mathcal{F}$.

A stochastic process on a probability space $(\Omega, \mathcal{F}, P)$ is a parametrized collection of random variables $\{Y_t\}_{t \in T}$. For the purposes of this thesis $T = [0, \infty)$ and corresponds to time. For a fixed t, Y_t is a random variable $\omega \to Y_t(\omega)$, with $\omega \in \Omega$, since random variables are, by definition, functions from the set of outcomes Ω to some other set. Fixing ω, on the other hand, yields a function $t \to Y_t(\omega)$, which corresponds to the time evolution of the stochastic process for a given ω. An important example of a stochastic process is the *Wiener process* W_t, which is a continuous time stochastic process satisfying the following:

1. $W_0 = 0$ almost surely.
2. $W_{t+dt} - W_t$ is independent of $\{W_s : s \leq t\}$, *i.e.* an increment of the Wiener process is independent of the earlier realisations of the process, so the Wiener process does not have a "memory" of its earlier behavior.
3. $W_{t+dt} - W_t$ is normally distributed with mean zero and variance dt.

4. W_t is continuous in time almost surely.

To numerically solve SDEs, an integral over a Wiener process must be defined. The usual definition of the Riemann-Stieltjes integral, for function $\mu(t)$ over the function $g(t)$, is

$$\int_{t_0}^{t} \mu(s)ds = \lim_{n\to\infty} \sum_{i=1}^{n} \mu(s_i^*)(g(s_i) - g(s_{i-1})), \tag{13}$$

where $s_i^* \in [s_{i-1}, s_i]$. For the Riemann-Stieltjes integral to exist, the limit of the sum must be same regardless of the choice of s_i^*. However, choosing $g(t)$ to be a Wiener process makes this impossible, and some other definition of the integral is required. In order to obtain an integral over a Wiener process, the set of functions, on which one such integral can be constructed, is defined next.

$(\mathcal{F}_{t_i})_{t_i \in T}$ is called a *filtration* of $\mathcal{F}$ if $\mathcal{F}_{t_i} \subset \mathcal{F}$, $\forall t_i$ and if $0 < t_i < t_j \Rightarrow \mathcal{F}_{t_i} \subset \mathcal{F}_{t_j}$ [23, p. 545]. An element $\mathcal{F}_{t_i}$ of a filtration $(\mathcal{F}_{t_i})_{t_i \in T}$ is the set of events up to time t_i and contains no information about the events at later times. A stochastic process Y_t is said to be *adaptive* with respect to filtration $(\mathcal{F}_{t_i})_{t_i \in T}$ if the random variable $Y_{t_i}(\omega) : \Omega \to \mathcal{F}_{t_i}$ is $\mathcal{F}_{t_i}$-measurable [22, p. 25]. This means that for all $a \in \mathcal{F}_{t_i}$ the set $A = \{\omega \in \Omega : Y_{t_i}(\omega) > a\}$ must be measurable, *i.e.* $A \subset \mathcal{F}_{t_i}$. In other words, random variable $Y_{t_i}(\omega)$ does not know anything of the realisations of the process Y_t at times $t > t_i$. This is because all values $Y_{t_i}(\omega) \in \mathcal{F}_{t_i}$ and $\mathcal{F}_{t_i}$ only contain information up to time t_i. Now define $\mathcal{V}$ as the set of $\mathcal{F}_{t_i}$ adapted functions $\mu(t, \omega)$ such that:

$$E\Big[\int_0^\infty \mu(t,\omega)^2 dt\Big] < \infty. \tag{14}$$

This set of functions is called the class of *square-integrable functions* and is the set of functions on which an integral over the Wiener process shall be defined. The importance of the square-integrability for the definition will be pointed out once the integral is constructed.

3.1 Stochastic Integrals and Itô Formula

The integral over a Wiener process, that will be derived here, is called the *Itô integral* and for a function μ is denoted:

$$\int_{t_0}^{t} \mu(s)dW_s, \tag{15}$$

where t_0 and t denote the lowest and highest times at which the Wiener process W_s is evaluated, respectively. The construction of the integral (15) given here follows closely Øksendal [22]. To define the Itô integral, so-called *elementary functions* $\phi \in \mathcal{V}$ are used:

$$\phi_n(t,\omega) = \sum_{j\geq 0}^{n} e_j(\omega)\cdot \mathcal{X}_{[t_j,t_{j+1})}(t). \tag{16}$$

Here, $\mathcal{X}$ denotes the indicator function, which is 1 on $[t_j, t_{j+1})$ and 0 elsewhere. The $e_j(\omega)$ are functions independent of t and, therefore, $\phi(t_n,\omega) = \phi(t,\omega)$ if $t \in [t_n, t_{n+1})$, *i.e.* $\phi(t,\omega)$ only takes discrete steps in time. The Itô integral of an elementary function is defined as:

$$\int_{t_0}^{t} \phi(s,\omega)dW_s = \sum_{j\geq 0}^{n} e_j(\omega)[W_{s_{j+1}} - W_{s_j}], \tag{17}$$

with $t_0 < s_j < s_{j+1} < t$. The Itô integral of a general function μ is then defined to be:

$$\int_{t_0}^{t} \mu(s,\omega)dW_t = \lim_{n\to\infty} \int_{t_0}^{t} \phi_n(s,\omega)dW_s, \tag{18}$$

where ϕ_n is a sequence of elementary functions such that:

$$E\Big[\int_{t_0}^{t} (\mu(s,\omega) - \phi_n(s,\omega))^2 ds\Big] \to 0, \tag{19}$$

as $n \to \infty$. The proof for existence of a suitable sequence ϕ_n can be found *e.g.* in Øksendal [22, p. 27]. Note, that existence of the limit requires $\mu \in \mathcal{V}$.

However, the Itô integral is not the only feasible way to define an integral over a Wiener process. Another such an integral is the *Stratonovich integral* denoted by

$$\int_{t_0}^{t} \mu(s,\omega) \circ dW_s.$$

This integral is defined using the mean square limit of a sequence of random variables. Y is said to be the mean square limit, or L^2-limit, of the sequence of random variables Y_n if

$$\lim_{n\to\infty} E\big[(Y_n - Y)^2\big] = 0. \tag{20}$$

The Stratonovich integral of function $\mu(t,\omega)$ is defined as the L^2-limit of:

$$Y_n = \sum_{i=0}^{n-1} \frac{\mu(s_{i+1},\omega) + \mu(s_i,\omega)}{2}(W_{s_{i+1}} - W_{s_i}). \tag{21}$$

Both Itô and Stratonovich integrals can be understood as a limit of

$$\sum_{i\geq 1} \mu(t^*,\omega)(W_{t_{j+1}} - W_{t_j}), \tag{22}$$

but in Itô's case $t^* = t_j$ whereas for Stratonovich $t^* = (t_{j+i} + t_j)/2$. The main advantage of the Stratonovich integral is that it conforms to most integration rules of the usual Riemann integral while Itô integral does not. The Itô integral's main advantage, on the other hand, is its *martingale* property [22, p. 31]. This means that for a filtration $\mathcal{F}_t$ the Itô integral I_t satisfies

$$E[I_s|\mathcal{F}_t] = I_t, \forall s \geq t, \tag{23}$$

i.e. the expectation value of the integral for time $t \geq s$ is the value of the integral at time s. As an illustrative example of a martingale, consider a fair game, *i.e.* a game with an equal chance of winning or losing a certain amount of money. A player's capital in such a game is a martingale: in the beginning of each round of playing, the expected value of the capital after that round is the same as the current capital of the player. The martingale property allows application of a wide set of results from probability theory to Itô integrals.

A disadvantage of the Itô integral is that it does not follow the rules of Riemann integration. Therefore, to evaluate the integrals without going back to first principles, and to derive schemes to numerically evaluate Itô integrals, a result called Itô's formula, or Itô's lemma, is required. Itô's lemma is the generalisation of the fundamental theorem of calculus to cover stochastic processes. It is a result for a so-called Itô drift-diffusion process X_t, defined as $X_t = X_{t_0} + \int_{t_0}^{t} f(X_s)ds + \int_{t_0}^{t} g(X_s)dW_s$, where $f(X_s)$ describes drift and $g(X_s)$ diffusion. To start with, consider the Taylor expansion of a C^2-function $h(X_t, t)$:

$$h(X_t, t) = h(X_{t_0}, t_0) + \sum_j \Delta h(\Delta X_j, \Delta t_j) \tag{24}$$

$$= h(X_{t_0}, t_0) + \sum_j \frac{\partial h}{\partial t}\Delta t_j + \sum_j \frac{\partial h}{\partial X}\Delta X_j \tag{25}$$

$$+ \frac{1}{2}\sum_j \frac{\partial^2 h}{\partial t^2}(\Delta t_j)^2 + \frac{1}{2}\sum_j \frac{\partial^2 h}{\partial t \partial X}(\Delta t_j)(\Delta X_j) + \frac{1}{2}\sum_j \frac{\partial^2 h}{\partial X^2}(\Delta X_j)^2 + \mathcal{O}(\Delta t_j^2). \tag{26}$$

As $\Delta t_j \to 0$, the increments become differentials and the sums integrals. The terms of order greater then $\mathcal{O}(dt)$ can be assumed small. $dX^2 = (f(X)dt + g(X)dW_t)^2$ contains a term of order $\mathcal{O}((dW_t)^2)$. Since increments of a Wiener process have variance proportional to the time difference between the starting and endpoints of the increment, *i.e* $(dW)^2 \propto \mathcal{O}(dt)$, it follows that $dW_t \propto \mathcal{O}(\sqrt{dt})$. Therefore, the $\mathcal{O}((dW_t)^2)$ term is of order $\mathcal{O}(dt)$ and does not disappear. Denoting $\frac{\partial h[X(t),t]}{\partial X(t)} = h'[X(t), t]$ and $\frac{\partial h[X(t),t]}{\partial t} = h_t[X(t), t]$, one obtains

$$h[X(t), t] - h[X(t_0), t_0] = \int_{t_0}^{t} \Big(h_s[X(s), s] + \frac{1}{2}h''[X(s), s]\Big)ds + \int_{t_0}^{t} h'[X(s), s]dW_s, \tag{27}$$

which is the Itô formula. Note, that an extra term $\frac{1}{2}h''[X(s),s]$ is present in the Itô formula, but does not appear in the fundamental theorem of calculus. Setting $h[X(t),t] = X(t)$ now yields

$$X(t) - X(t_0) = \int_{t_0}^{t} f(X(s))ds + \int_{t_0}^{t} g(X(s))dW_s \tag{28}$$

Discretising Eq. (28) leads to

$$X_{n+1} = X_n + f_n\Delta t + g_n\Delta W, \tag{29}$$

where the index n denotes the value of a function at time t_n, $\Delta t = t_{n+1} - t_n$ and $\Delta W = W_{t_{n+1}} - W_{t_n}$. This is the Euler-Maruyama method and the simplest numerical scheme to solve SDEs.

To analyze the accuracy of a stochastic numerical scheme, two types of convergence can be applied: weak and strong. In the deterministic limit, *i.e.* for an ordinary differential equation, the two convergences become the same. A numerical scheme is said to converge weakly with order p_{weak}, if, for a function of polynomial growth h, there exists a constant C such that

$$E\big[\|h(X(t_n)) - h(X_n)\|\big] \leq C(\Delta t)^{p_{weak}}, \tag{30}$$

for all $\Delta t < \epsilon$, with $\epsilon > 0$ and $p > 0$ as large as possible [24, p. 327]. Weak convergence, *i.e.* that the LHS of Eq. (30) approaches zero as $\Delta t \to 0$, is sufficient for the numerical approximation of the distribution function to converge towards the exact distribution. In other words, the weak convergence only tells, that a numerical scheme converges in distribution or, in a sense, "on average". The weak order of convergence does not state the convergence of paths of individual processes X_t. To have a measure of the accuracy for the path of a particular stochastic process, when using a numerical method, the strong convergence is required. A numerical method is said to converge with strong order p if, for fixed Δt, there exists $C > 0$ such that [24, p. 323]

$$E\big[\sup_{t_n<T} \|X(t_n) - X_n\|\big] \leq C(\Delta t)^p, \tag{31}$$

For a numerical method to converge strongly, LHS of Eq. (31) has to approach zero as $\Delta t \to 0$. The strong convergence tells whether the numerically obtained path of a process X_t converges to the actual path of the process or not. In other words, strong order of convergence is a measure of convergence in probability. The Euler-Maryuama method can be shown to have weak order of convergence of 1 and strong order of convergence 1/2 for "well-behaving" f and g. The convergence of an adaptive numerical method, as the time step approaches zero, can only be guaranteed when strong order of convergence is at least 1 [25]. Therefore, some method other than Euler-Maruyama is required for an adaptive scheme.

3.2 Milstein Method

To obtain a numerical method with strong order of convergence of 1, Itô's formula (28) has to be applied to both $f(X(t))$ and $g(X(t))$, denoted f_t and g_t for brevity, in an Itô drift-diffusion process. Noting that $\partial X(t)/\partial t = f(X(t))$ and $\partial X(t)/\partial W = g(X(t))$ this results in

$$f_s - f_{t_0} = \int_{t_0}^{s} (f'_u f_u + \frac{1}{2} f''_u g_u^2) du + \int_{t_0}^{s} (f'_u g_u) dW_u, \tag{32}$$

$$g_s - g_{t_0} = \int_{t_0}^{s} (g'_u f_u + \frac{1}{2} f''_u g_u^2) du + \int_{t_0}^{s} (g'_u g_u) dW_u. \tag{33}$$

These results can be substituted into Eq. (28), resulting in

$$X(t) - X(t_0) = \int_{t_0}^{t} \Big(\int_{t_0}^{s} (f'_u f_u + \frac{1}{2} f''_u g_u^2) du + \int_{t_0}^{s} (f'_u g_u) dW_u + f_{t_0} \Big) ds \tag{34}$$

$$+ \int_{t_0}^{t} \Big(\int_{t_0}^{s} (g'_u f_u + \frac{1}{2} f''_u g_u^2) du + \int_{t_0}^{s} (g'_u g_u) dW_u + g_{t_0} \Big) dW_s. \tag{35}$$

Now terms with $duds \propto \mathcal{O}(dt^2)$ and $dudW_s \propto \mathcal{O}(dt^{3/2})$ are set to zero leaving

$$X(t) - X(t_0) \approx f_{t_0} \int_{t_0}^{t} ds + g_{t_0} \int_{t_0}^{t} dW_s + \int_{t_0}^{t} \int_{t_0}^{s} (g'_u g_u) dW_u dW_s. \tag{36}$$

If $t - t_0$ is small the last term can be approximated as

$$\int_{t_0}^{t} \int_{t_0}^{s} (g'_u g_u) dW_u dW_s \approx g'_{t_0} g_{t_0} \int_{t_0}^{t} \int_{t_0}^{s} dW_u dW_s. \tag{37}$$

The integral part of (37) can now be evaluated, resulting in

$$\int_{t_0}^{t} \int_{t_0}^{s} dW_u dW_s = \int_{t_0}^{t} (W_s - W_{t_0}) dW_s \tag{38}$$

$$= \int_{t_0}^{t} W_s dW_s - W_{t_0}(W_t - W_{t_0}). \tag{39}$$

Itô's formula (28) can be applied to the remaining integral by setting $X(s) = W_s$:

$$\int_{t_0}^{t} W_s dW_s = \frac{1}{2} W_t^2 - \frac{1}{2} W_{t_0}^2 - \frac{1}{2} \int_{t_0}^{t} ds. \tag{40}$$

Thus one obtains

$$X(t) - X(t_0) = f_{t_0} \int_{t_0}^{t} ds + g_{t_0} \int_{t_0}^{t} dW_s \tag{41}$$

$$+ g'_{t_0} g_{t_0} \big(\frac{1}{2} W_t^2 - \frac{1}{2} W_{t_0}^2 - \frac{1}{2}(t - t_0) - W_{t_0}(W_t - W_{t_0}) \big) \tag{42}$$

$$= f_{t_0} \int_{t_0}^{t} ds + g_{t_0} \int_{t_0}^{t} dW_s + \frac{1}{2} g'_{t_0} g_{t_0} \big((W_t - W_{t_0})^2 - (t - t_0) \big) \big), \tag{43}$$

which can be discretized to obtain the Milstein method [24, p. 345]

$$X_{n+1} = X_n + f_n \Delta t + g_n \Delta W + \frac{1}{2} g'_n g_n (\Delta W^2 - \Delta t), \tag{44}$$

where $X_n = X(t_n)$, $\Delta t = t_{n+1} - t_n$ and $\Delta W = W_{t_{n+1}} - W_{t_n}$. To collect all drift terms together, Milstein method can be rewritten as

$$X_{n+1} = X_n + f^*(X_n)\Delta t + g(X_n)\Delta W + \frac{1}{2} g'(X_n) g(X_n) (\Delta W)^2, \tag{45}$$

where $f^*(X) = f(X) - \frac{1}{2} g'(X) g(X)$. Milstein method can be shown to have strong order of convergence 1 [24, p. 345], guaranteeing the convergence of the numerical solution to the exact solution as $\Delta t \to 0$. Thus, the scheme is suitable for following individual stochastic processes with an adaptive time-stepping scheme.

Next, the use of Milstein scheme with adaptive time stepping is examined. To achieve this, the two-way error checking proposed by Lamba [26] can be used. The error estimates enable to determine when a sufficiently short time step is found for the adaptive scheme. One of the error estimates is used for situations where diffusion dominates over drift. The other is used in the opposite case. To start with the diffusion error estimate, consider the Stratonovich-Taylor expansion of an Itô diffusion process X, which can be written down as [24, p. 188]

$$X_{n+1} = X_n + f^* J_0 + g J_1 + g g' J_{11} \tag{46}$$

$$+ J_{10} f^{*\prime} g + J_{01} g' f + \frac{1}{6} g'' g g + \frac{1}{6} J_1^3 (g')^2 g + \mathcal{O}((\Delta t)^2), \tag{47}$$

with

$$\begin{aligned} \mathrm{J}_0 &= \textstyle\int_{t_n}^{t_n+\Delta t} ds, \\ \mathrm{J}_1 &= \textstyle\int_{t_n}^{t_n+\Delta t} \circ dW_s = \Delta W, \\ \mathrm{J}_{10} &= \textstyle\int_{t_n}^{t_n+\Delta t} \int_{t_n}^{s_1} \circ dW_s ds_1, \\ \mathrm{J}_{01} &= \textstyle\int_{t_n}^{t_n+\Delta t} \int_{t_n}^{s_1} ds \circ dW_{s_1}, \\ \mathrm{J}_{11} &= \textstyle\int_{t_n}^{t_n+\Delta t} \int_{t_n}^{s_1} \circ dW_s \circ dW_{s_1}. \end{aligned} \tag{48}$$

Eq. (47) is the integral form of a Taylor expansion, but written down using Stratonovich integrals instead of Itô ones. The first four terms of Eq. (47) are the Milstein method, and the remaining terms form its truncation error

$$\epsilon = J_{10}f^{*\prime}g + J_{01}g'f + \frac{1}{6}J_1^3 g''g^2 + \frac{1}{6}J_1^3(g')^2 g + \mathcal{O}((\Delta t)^2). \tag{49}$$

Since the second last term in (49) can be written using ΔW, g' and g, which have already been calculated for the Milstein step, Lamba assumes controlling this term leads to an acceptable control of the local error. Thus, the first error estimate can be defined as

$$E_g(X_n, \Delta t) = \frac{1}{6}|\Delta W^3(g')^2 g|, \tag{50}$$

which is an upper bound for the term. A second error estimate is required, however, since the first one does not depend on the drift term f of the original SDE. Therefore, Lamba proposes another error estimate for the low-diffusion regime which requires the so-called Heun method, *i.e.*

$$X_{n+1} = X_n + \frac{\Delta t}{2}(f(X_n) + f(X_{n+1})) \tag{51}$$

$$= X_n + \frac{\Delta t}{2}(f(X_n) + f(X_n + \Delta t f(X_n))), \tag{52}$$

where $dX/dt = f(X)$. The low-diffusion error corresponds to the difference between the Euler and Heun methods, and an upper bound for this difference is

$$E_f(X_n, \Delta t) = |\frac{\Delta t}{2}(f(X_n + \Delta t f(X_n)) - f(X_n))|. \tag{53}$$

With the two error estimates in place, Milstein method can be used with adaptive time-stepping.

3.3 Adaptive Wiener Process Generation

When generating Wiener process values using an adaptive time stepping scheme, one has to be careful. A Wiener process value has to be generated for every attempted time step. However, if a time step is rejected, the Wiener process value for that given time step cannot be forgotten because it will affect the Wiener process realisations at earlier times. Considering the covariance of a Wiener process at different times, one may state

$$\mathrm{Cov}[W_s, W_s] = \mathrm{Var}[W_s], \tag{54}$$

and let $s < t$. Then, the increments $W_t - W_s$ are independent of the values of W_s and W_t. Therefore

$$\mathrm{Cov}[W_s, W_t] = \mathrm{Cov}[W_s, W_s + (W_t - W_s)] \tag{55}$$

$$= \mathrm{Cov}[W_s, W_s] + \mathrm{Cov}[W_s, W_t - W_s] \tag{56}$$

$$= s + 0. \tag{57}$$

For arbitrary t_i and t_j, $\mathrm{Cov}[W_{t_i}, W_{t_j}] = \min(t_i, t_j)$. One can consider a Wiener process at times $0 < t_1 < ... < t_k$ and t such that $t_i < t < t_{i+1}$ with $i \in \{1, 2, ..., k-1\}$. Since increments to the Wiener process are independent of the values of the process, W_t only depends on W_{t_i} and $W_{t_{i+1}}$. The values of a Wiener process are normally distributed, so the three values at t_i, t and t_{i+1} together form a multivariate normal distribution

$$\begin{pmatrix} W_t \\ W_{t_i} \\ W_{t_{i+1}} \end{pmatrix} \sim N\left(0, \begin{pmatrix} t & t_i & t \\ t_i & t_i & t_i \\ t & t_i & t_{i+1} \end{pmatrix} \right), \tag{58}$$

where the matrix is the covariance matrix of the distribution. To determine the expectation and variance of W_t for given W_{t_i} and $W_{t_{i+1}}$, one can now use the conditioning formula

$$\begin{pmatrix} X_1 \\ X_2 \end{pmatrix} \sim N\left(\begin{pmatrix} \mu_1 \\ \mu_2 \end{pmatrix}, \begin{pmatrix} \Sigma_{11} & \Sigma_{12} \\ \Sigma_{21} & \Sigma_{22} \end{pmatrix} \right) \tag{59}$$

$$\Rightarrow (X_1 | X_2 = x) \sim N(\mu_1 + \Sigma_{12}\Sigma_{22}^{-1}(x - \mu_2), \Sigma_{11} - \Sigma_{12}\Sigma_{22}^{-1}\Sigma_{21}), \tag{60}$$

for two normally distributed random variables X_1 and X_2 with means μ_1 and μ_2, respectively, and covariance matrix Σ [23, p. 65]. Setting $W_{t_i} = a$ and $W_{t_{i+1}} = b$ gives the following conditional expectation for W_t [23, p. 84]

$$E[W_t | W_{t_i} = a, W_{t_{i+1}} = b] = 0 - \begin{pmatrix} t_i & t \end{pmatrix} \begin{pmatrix} t_i & t_i \\ t_i & t_{i+1} \end{pmatrix}^{-1} \begin{pmatrix} a \\ b \end{pmatrix} \tag{61}$$

$$= -\frac{1}{t_{i+1} - t_i} \begin{pmatrix} t_i & t \end{pmatrix} \begin{pmatrix} t_{i+1}/t_i & -1 \\ -1 & 1 \end{pmatrix}^{-1} \begin{pmatrix} a \\ b \end{pmatrix} \tag{62}$$

$$= \frac{(t_{i+1} - t)a + (t - t_i)b}{(t_{i+1} - t_i)}, \tag{63}$$

and

$$\mathrm{Var}[W_t | W_{t_i} = a, W_{t_{i+1}} = b] = t - \frac{1}{t_{i+1} - t_i} \begin{pmatrix} t_i & t_{i+1} \end{pmatrix} \begin{pmatrix} t_{i+1}/t_i & -1 \\ -1 & 1 \end{pmatrix}^{-1} \begin{pmatrix} t_i \\ t \end{pmatrix} \tag{64}$$

$$= \frac{(t_{i+1} - t)(t - t_i)}{(t_{i+1} - t_i)}, \tag{65}$$

for conditional variance. Note that the conditional expectation depends linearly on t and approaches a as $t \to t_i$ and b as $t \to t_{i+1}$. Note also that the variance decreases close to the "tying-down points" t_i and t_{i+1}, due to continuity of a Wiener process. A Wiener process W_t, which is "tied down" like this, is called a Brownian bridge (Fig. 4).

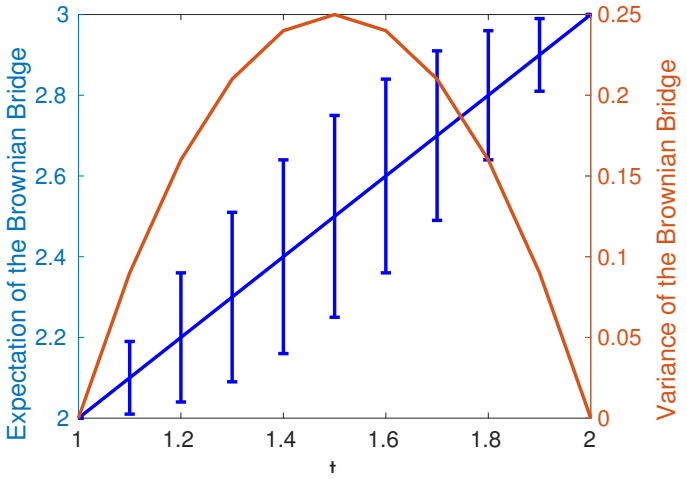

Figure 4: An illustration of a Brownian bridge from $t_i = 1$ to $t_{i+1} = 2$ with $a = 2$ and $b = 3$. The blue curve represents the expectation value and the error bars the standard deviation of Brownian bridge at given times. The red curve represents the variance of the Brownian Bridge at given times.

There are two cases for the generation of Wiener process for an SDE, depending on the length of the new time step. First consider $t_n + \Delta t > t_{max}$, where t_n is the time the integration itself has reached so far and t_{max} is the maximum time a generated Wiener process value exists. In this case, where there are no future Wiener process values yet, the new value can be generated with $W(t_n + \Delta t) - W(t_{max})$ normally distributed with $\mu = 0$ and $\sigma^2 = t_n + \Delta t - t_{max}$. If $t_n + \Delta t < t_{max}$, the Brownian bridge must be used with t_- and t_+ chosen in such a way that Wiener process values exist at these two points, but nowhere in the intervals $(t_-, t_n + \Delta t)$ or $(t_n + \Delta t, t_+)$.

To understand the adaptive time-stepping process, one may suppose that the integration has reached time t_n and no Wiener process values are known for later times. A time step Δt_1 is then chosen and the Wiener process is evaluated at $t_n + \Delta t_1$. After this, the error estimates are made for Δt_1. If one of the errors is too large, a shorter time step Δt_2 is chosen. However, Brownian bridge must now be used to determine the value of the Wiener process, for a Wiener process value exists for a later time $(t_n + \Delta t_1)$. The above process is then repeated. If the new errors are small enough, $t_{n+1} = t_n + \Delta t_2$ becomes the new time the integration has reached and the Wiener process value at t_n can be dismissed. However, for the next time step, the Wiener process value at $t_n + \Delta t_1$ must be preserved. If the next attempted time step reaches beyond $t_n + \Delta t_1$, Wiener process generation without Brownian bridge must be used, as described in the previous paragraph. Otherwise, Brownian bridge is used.

4 ASCOT and Milstein Method with Adaptive Time-Stepping

In order to describe the implementation of Milstein method with adaptive time-stepping to ASCOT, the basic working principles of the code are described. ASCOT seeks to find a distribution function $f(\mathbf{z}, t)$, where $\mathbf{z}$ are the phase space coordinates and t is the time of a particle population in a background plasma [4]. The distribution function should satisfy the kinetic equation

$$\frac{\partial f}{\partial t} + \dot{\mathbf{z}} \cdot \frac{\partial f}{\partial \mathbf{z}} = \left(\frac{\partial f}{\partial t}\right)_{coll}. \tag{66}$$

If the RHS of the kinetic equation (66) is set to zero, the remaining Vlasov equation describes the collisionless, or Hamiltonian, part of the motion of the particles. This collisionless motion is given by the Lorentz force and Maxwell's equations and is deterministic. The collisions, described by the collision operator $(\partial f/\partial t)_{coll}$, consist of friction and diffusion terms and, when included, make the motion stochastic.

In complex systems, the kinetic equation (66) cannot be solved directly. The motion can be found, however, with a Monte Carlo method. The motion of an individual particle from a population with distribution function $f(\mathbf{z}, t)$ can be described by a SDE, known as the Langevin equation

$$d\mathbf{z} = (\dot{\mathbf{z}} + \mathbf{a}(\mathbf{z}, t))dt + \boldsymbol{\sigma}(\mathbf{z}, t) \cdot d\mathbf{W}, \tag{67}$$

where the coefficients $\mathbf{a}$ and σ can be derived. Summing over the individual paths given by Langevin equation yields the distribution function.

In most cases the simulations can be greatly accelerated by averaging out the rapid spiralling of a charged particle around magnetic field lines and considering only the motion of the "centre of mass" of the gyro-motion, or guiding-centre (GC). GC corresponds to a coordinate transformation from the particle phase space to the guiding-centre phase space and this transformation is valid when physical quantities remain close to constant during one gyro-period. In the particle phase space, three spatial and three velocity coordinates need to be considered, whereas in the guiding-centre phase space, it is possible to work with only five coordinates by omitting the gyro-angle: the angle between the guiding-centre and the full orbit. [27] In this chapter, the exact form of the collision operator in ASCOT is presented and used to derive GC Langevin equation. The Milstein method and adaptive time-stepping scheme are then applied to this equation.

4.1 Fokker-Planck Collision Operator

For the description of ASCOT's collision operator, one can start by considering a collision operator $C[f]$ of the form [28]

$$C[f] = -\frac{\partial}{\partial \dot{\mathbf{z}}}(\mathbf{a}f) + \frac{\partial}{\partial \dot{\mathbf{z}}}\frac{\partial}{\partial \dot{\mathbf{z}}} : (\mathbf{D}f). \tag{68}$$

One can rewrite the kinetic equation (66) as the Fokker-Planck equation

$$\frac{\partial}{\partial t}f(\mathbf{z},t) = -\frac{\partial}{\partial \mathbf{z}} \cdot [\dot{\mathbf{z}} + \mathbf{a}(\mathbf{z},t)f(\mathbf{z},t)] + \frac{\partial}{\partial \mathbf{z}}\frac{\partial}{\partial \mathbf{z}} : [\mathbf{D}(\mathbf{z},t)f(\mathbf{z},t)], \tag{69}$$

where $\mathbf{a}$ is a friction coefficient and $\mathbf{D}$ is a diffusion coefficient. The Fokker-Planck form of the kinetic equation can be used to show the connection between the kinetic equation (66) and the Langevin equation (67) [29].

To determine the coefficients $\mathbf{D}$ and $\mathbf{a}$, the nature of scattering of charged particles between each other must be considered. In a fully ionized plasma, the particles interact with each other via Coulomb interaction. In these Coulomb collisions, any charged particle is constantly scattering with all other particles within its Debye sphere. In most circumstances, this scattering only has a small effect on the particle's trajectory [30, p. 54]. For the derivation of the Fokker-Planck friction and diffusion coefficient, the Coulomb collisions are assumed to be such "small angle collision". Furthermore, the Coulomb collisions only affect a particle's velocity. Therefore, the position $\mathbf{x}$ components of $\mathbf{a}$ and $\mathbf{D}$ become zero and only velocity $\mathbf{v}$ components of the coefficients need to be considered. This leads to the following expressions for $\mathbf{D}$ and $\mathbf{a}$:

$$\mathbf{a}(\mathbf{v}) = \frac{1}{\tau}\langle \Delta \mathbf{v} \rangle \tag{70}$$

$$\mathbf{D}(\mathbf{v}) = \frac{1}{\tau}\langle \Delta \mathbf{v} \Delta \mathbf{v} \rangle, \tag{71}$$

where $\mathbf{v}$ is the particle velocity, $\Delta\mathbf{v}$ is the change in the particle velocity due to one collision, τ is the duration of a collision, and $\langle \Delta \mathbf{v} \rangle$ describes the average change in the velocity of the whole particle population. $\mathbf{D}$ is related to σ in Langevin equation (67) via

$$\mathbf{D} = \frac{1}{2}\boldsymbol{\sigma}\boldsymbol{\sigma}^T. \tag{72}$$

When collisions are small-angle Coulomb collisions, $\mathbf{D}$ and $\mathbf{a}$ take the forms [31, p. 25]

$$\mathbf{a} = -\sum_b \frac{c_{ab}}{m_a^2}\left(1 + \frac{m_a}{m_b}\right)\int d\mathbf{v}' f_b(\mathbf{v}')\frac{\mathbf{u}}{u^3} \tag{73}$$

$$\mathbf{D} = \frac{1}{2}\sum_b \frac{c_{ab}}{m_a^2}\int d\mathbf{v}' f_b(\mathbf{v}')\left(\frac{\mathbf{I}}{u} - \frac{\mathbf{uu}}{u^3}\right) \tag{74}$$

for collisions of plasma species a. The sum is over all plasma species b, $\mathbf{u} = \mathbf{v} - \mathbf{v}'$ and $c_{ab} = q_a^2 q_b^2 \ln\Lambda / 4\pi(\epsilon_0)^2$, where ϵ_0 is the permittivity of free space, $\ln\Lambda$ the Coulomb logarithm and m_a and q_a are the mass and charge of species a, respectively.

Assuming that the background plasma is isotropic, the diffusion tensor has longitudinal and transverse projection tensors with respect to $\mathbf{v}$ and can be written as a linear combination of them as [28, p. 76]

$$\mathbf{D}(\mathbf{v}) = D_{\parallel}(v)\frac{\mathbf{vv}}{v^2} + D_{\perp}(v)\left(\mathbf{I} - \frac{\mathbf{vv}}{v^2}\right). \tag{75}$$

From Eqs. (73), (74) and (75), $D_{\parallel}$ and $D_{\perp}$ can be calculated explicitly when the background plasma is assumed to be Maxwellian, *i.e.*

$$f_b = \frac{n_b}{\pi^{3/2}v_b^2}\exp(-v^2/(2T_b/m_b)), \tag{76}$$

where T_b is the temperature of plasma species b. Note, that temperature is assumed to have the units of energy. $D_{\parallel}(v)$ can then be determined from Eq. (74) and is

$$D_{\parallel} = \sum_b \frac{1}{2}\frac{c_{ab}n_b}{m_a^2 v} G\left(\frac{v}{\sqrt{2T_b/m_b}}\right), \tag{77}$$

where

$$G(x) = \frac{\mathrm{erf}(x) - x\mathrm{erf}'(x)}{2x^2}, \tag{78}$$

with $\mathrm{erf}(x)$ being the error function. The perpendicular diffusion coefficient $D_{\perp}$ can be solved from Eq. (75) by substituting from Eq. (77) to obtain

$$D_{\perp} = \sum_b \frac{1}{2}\frac{c_{ab}n_b}{{}^2_a v}\left(\mathrm{erf}\left(\frac{v}{\sqrt{2T_b/m_b}}\right) - \frac{1}{2}G\left(\frac{v}{\sqrt{2T_b/m_b}}\right)\right). \tag{79}$$

Under the assumption of an isotropic, Maxwellian background plasma, the friction coefficient becomes

$$\mathbf{a} = \left(1 + \frac{m_b}{m_a}\right)\nu\mathbf{v}, \tag{80}$$

where ν is the characteristic collision frequency and has the form

$$\nu = \sum_b \frac{c_{ab}n_b}{2T_b m_a}\frac{G(v/\sqrt{2T_b/m_b})}{v}, \tag{81}$$

The Langevin equation (67) is for the gyro-orbit motion of a particle and, therefore, it has to be transformed to the guiding-center phase space before implementing it in ASCOT.

4.2 Guiding-Centre Langevin Equation

The guiding-centre transformation corresponds to a coordinate transformation $\mathbf{x} = \mathbf{X} + \boldsymbol{\rho}$, where $\mathbf{x}$ is the particle's position, $\mathbf{X}$ is the position of the particle's guiding-centre and $\boldsymbol{\rho}$ is the particle's Larmor radius. A similar, but less intuitive, transformation is made for the velocity coordinates as well. Obtaining such a transformation can be done using Lie-transform techniques. The guiding-centre transformation of the kinetic equation with a Fokker-Planck collision operator, used in ASCOT, was first done by Brizard [32]. The guiding-centre Fokker-Planck equation is

$$\frac{\partial \mathcal{F}}{\partial t} + \dot{\mathcal{Z}}^\alpha \frac{\partial \mathcal{F}}{\partial \mathcal{Z}^\alpha} = -\frac{1}{\mathcal{J}} \frac{\partial}{\partial \mathcal{Z}^\alpha} \left[\mathcal{J} \left(\mathcal{K}^\alpha \mathcal{F} - \mathcal{D}^{\alpha\beta} \frac{\partial \mathcal{F}}{\partial \mathcal{Z}^\beta} \right) \right], \tag{82}$$

where $\mathcal{Z}^\alpha$ are the guiding-centre phase space coordinates, $\dot{\mathcal{Z}}^\alpha$ their time derivatives, $\mathcal{J}$ the GC phase space Jacobian and $\mathcal{K}^\alpha$ and $\mathcal{D}^{\alpha\beta}$ the GC friction and diffusion tensors, respectively. When using the guiding-centre transformation, physical quantities inside the Larmor radius are assumed constant, and the gyro-angle can be dismissed. The guiding-centre coordinates can then be chosen as $(\mathbf{X}, v, \xi)$, where v is the particle speed and ξ is pitch, *i.e.* the ratio of speed parallel to the magnetic field and total speed. With this choice of coordinates, one obtains [33]

$$\mathcal{D}^{\alpha\beta} = \begin{pmatrix} \mathcal{D}^{\mathbf{XX}} & 0 & 0 \\ 0 & D_\parallel & 0 \\ 0 & 0 & (1-\xi^2)\frac{D_\perp}{v^2} \end{pmatrix} \tag{83}$$

$$\mathbf{K}^\alpha = \begin{pmatrix} \mathbf{0} \\ -\nu v \\ 0 \end{pmatrix}, \tag{84}$$

Assuming $\partial \mathcal{J}/\partial t = 0$, *i.e.* stationary background, the motion of individual particles in the guiding-centre picture obeying the GC kinetic equation (Eq. (82)) is described by the following Langevin equation

$$d\mathcal{Z}^\alpha = \mathcal{A}^\alpha dt + \Sigma^{\alpha\beta} d\mathcal{W}^\beta, \tag{85}$$

with

$$\mathcal{D}^{\alpha\beta} = \frac{1}{2} \Sigma^{\alpha\gamma} \Sigma^{\beta\gamma}, \tag{86}$$

$$\mathcal{A}^\alpha = \dot{\mathcal{Z}}^\alpha + \mathbf{K}^\alpha + \frac{1}{\mathcal{J}} \frac{\partial}{\partial \mathcal{Z}^\beta} (\mathcal{J} \mathcal{D}^{\alpha\beta}), \tag{87}$$

where $\dot{\mathcal{Z}}^\alpha$ contains the equations of motion of GC without collisions. Since $\mathcal{D}^{\alpha\beta}$ was block-diagonal (Eq. (83)), $\Sigma^{\alpha\beta}$ is also block-diagonal. This means that the Langevin equations for pitch and velocity are independent of each other and independent of

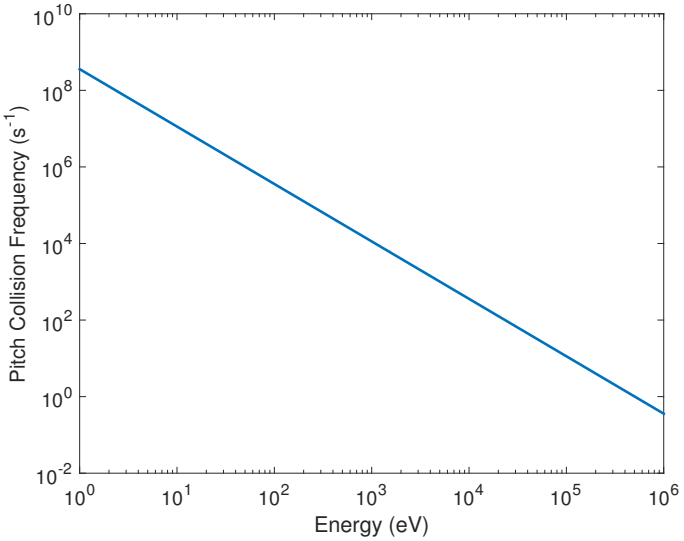

Figure 5: Pitch collision frequency of helium in a deuterium-tritium plasma ($n_e = 4.5 \times 10^{19}\mathrm{m}^{-3}$, $n_i = 2 \times 10^{19}\mathrm{m}^{-3}$, $T_i = 10\mathrm{keV}$, $T_e = 10\mathrm{keV}$).

the Langevin equations for the GC spatial coordinates, enabling the use of one-dimensional Milstein method.

The three independent Langevin equations for GC location, pitch and velocity make the following contributions to the particle transport: the location equation corresponds to the classical transport, the pitch equation to neoclassical transport, and the velocity equation, which only changes the energy of the particles, does not contribute to the transport directly. However, the velocity equation contributes to the widening of particle orbits. In most tokamaks, neoclassical diffusion is at least an order of magnitude larger than classical diffusion and, thus, the spatial diffusion can be assumed small. Under this assumption and considering v and ξ only, one obtains the following equations:

$$d\xi = \left(\dot{\xi} - \xi\frac{2D_\perp}{v^2}\right)dt + \sqrt{(1-\xi^2)\frac{2D_\perp}{v^2}}dW_t \tag{88}$$

$$dv = \left(\dot{v} - \nu v + \frac{\partial D_\parallel}{\partial v} + 2\frac{D_\parallel}{v}\right)dt + \sqrt{2D_\parallel}dW_t, \tag{89}$$

where $\dot{p}$ and $\dot{\xi}$ correspond to the Hamiltonian motion of the particles. The quantity $-2D_\perp/v^2$ is the so-called pitch collision frequency. Figure 5 shows that this frequency decreases heavily as the energy increases. Therefore, when simulating the slowing-down of these particles, a longer time step can be used than for particles with lower energies, making a case for the adaptive time-stepping for slowing-down simulations.

4.3 Implementing Adaptive Time-Stepping to ASCOT

In earlier ASCOT implementation, ΔW_t was obtained from $\Delta W_t = \pm\sqrt{\Delta t}$, with ± 1 randomly chosen. Usually, this is a sufficient approximation for a normally distributed random variable with mean 0 and variance Δt. However, this approximation would lead to the elimination of the last term of Milstein method (44). To avoid this, the Box-Müller transform can be used [34]. In this transform, two uniformly distributed random variables, u_1 and u_2, are used to generate one standard normal random variable as

$$X_{standard} = \sqrt{-2\ln u_1}\cos 2\pi u_2, \tag{90}$$

which can be given the correct mean (μ) and variance (σ^2) by

$$\Delta W_t = \sigma X_{standard} + \mu. \tag{91}$$

The μ and σ are obtained from Eqs. (63) and (65). With Box-Müller as a final numerical modification, the algorithm for ASCOT's adaptive time-stepping becomes the following:

1. Start with an initial time step Δt

2. Generate ΔW_v using Box-Müller and Brownian bridge. Then calculate Δv with Milstein method, *i.e.*

$$\begin{aligned}\Delta v = &\left(-\nu v_n + \frac{1}{m^2}\left[\frac{\partial D_\parallel}{\partial v}\right]_n + \frac{2}{m^2}\frac{D_{\parallel,n}}{v_n}\right)\Delta t + \frac{1}{m}\sqrt{2D_{\parallel,n}}\Delta W_v \\ &+ \frac{1}{2m^2}\left[\frac{\partial D_\parallel}{\partial v}\right]_n ((\Delta W_v)^2 - \Delta t),\end{aligned} \tag{92}$$

where $D_{\parallel,n}$ and $(\partial D_\parallel/\partial v)_n$ denote the quantities $D_\parallel$ and $\partial D_\parallel/\partial v$ for $v = v_n$, respectively. Finally calculate the diffusion error (Eq. (50)) and deterministic error (Eq. (53)):

$$\epsilon_{Diff} = \frac{1}{6}\left|\Delta W_v^3 \frac{1}{m^3}\left[\frac{\partial D_\parallel}{\partial v}\right]_n^2 \frac{1}{\sqrt{2D_{\parallel,n}}}\right| \tag{93}$$

$$\epsilon_{Det} = \left|\frac{\Delta t}{2}(f(v_n + \Delta t f(v_n)) - f(v_n))\right|, \tag{94}$$

with

$$f(v) = -\nu v + \frac{1}{m^2}\frac{\partial D_\parallel}{\partial v} + \frac{2}{m^2}\frac{D_\parallel}{v} \tag{95}$$

3. Pick the maximum of the deterministic and diffusion errors (ϵ_{max}) and compare $err = \epsilon_{max}/\Delta v$ to a user-defined tolerance (tol). Set $\Delta t_v = \Delta t$.

4. If $err > tol$, reduce the time step by $\Delta t = \Delta t/2$ and return to step 2. Else, continue.

5. Generate ΔW_ξ using Box-Müller and Brownian bridge. Then calculate $\Delta\xi$ with Milstein method, *i.e.*

$$\begin{aligned}\Delta\xi = &-\xi_n \frac{2D_{\perp,n}}{v_n^2}\Delta t + \sqrt{(1-\xi_n^2)\frac{2D_{\perp,n}}{v_n^2}}\Delta W_\xi \\ &- \xi_n \frac{2D_{\perp,n}}{v_n^2}((\Delta W_\xi)^2 - \Delta t),\end{aligned} \tag{96}$$

   where $D_{\perp,n}$ denotes $D_{\perp,n}$ for v_n. Finally calculate the deterministic error:

$$\epsilon_{Det} = \left| -2\left(\frac{\Delta t D_{\perp,n}}{v_n^2}\right)^2 \right| \tag{97}$$

6. Set $err = \max(|\epsilon_{Det}/\Delta\xi|, \Delta\xi)$ and compare err to a user-defined tolerance (tol). The comparison $\epsilon_{Diff}/\Delta\xi$ is not done due to the singularity in ϵ_{Diff} at $\xi = \pm 1$. Set $\Delta t_\xi = \Delta t$.

7. If $err > tol$, reduce the time step by $\Delta t = \Delta t/2$ and return to step 5. Else, continue.

8. If $\Delta t_E \neq \Delta t_p$, go to step 2. This could happen if the time step was reduced further by the pitch collisions. In this case, ΔW_t must be evaluated again for energy. Due to the randomness of ΔW_t, the error for energy might occasionally become greater than the tolerance and the splitting of the step must continue. If $\Delta t_E = \Delta t_p$, continue.

9. Evaluate the collisions using Milstein method and time step Δt. Then set $\Delta t = 2\Delta t$ and return to step 2 for the next time step. It is worth noting how ASCOT deals with $\Delta\mathcal{E} = m\Delta v^2/2$, that would cause negative energy and $\Delta\xi$, that would cause $|\xi|$ to exceed 1. In both cases, reflective boundary conditions are used to prevent unphysical values from occurring.

Note that steps 2 and 5 require the generation of Wiener process values for Δv, $\Delta\xi$ and the error estimates. These Wiener process values must be stored and used for the Brownian bridge until the time of the simulated marker is past the time at which these values were generated.

4.4 Benchmarking the Adaptive Time-Stepping Scheme

Since the collision operator describes the friction and diffusion of a particle population in a Maxwellian background plasma, the energy distribution that can be derived from the velocity distribution should also eventually become Maxwellian. The pitch also eventually reaches the pitch distribution of the background plasma. Since the background was assumed isotropic, the pitch distribution also becomes uniform. To verify the energy and pitch distributions, 10 000 hydrogen test particles were run in a background plasma consisting of hydrogen and electrons with an equal temperature of 3 keV. The particles were simulated for one second in an axisymmetric magnetic background in JET. The energy distribution was sampled from a Maxwellian distribution (Fig. 6) with a probability of 97.18% using MATLAB's `chi2gof` goodness-of-fit test [35]. The pitch distribution was sampled from a uniform distribution with probability 71.0% (Fig. 7.a) using the same goodness-of-fit test.

The use of Brownian bridge and adaptive time-stepping solved an important issue in previous versions of ASCOT's pitch collision operator. Omitting Brownian bridge in the adaptive Wiener process generation results in a distribution biased towards $\xi = \pm 1$ (Fig. 7.b). This is because the absolute value of expectation value of Δt is greatest for a given time step at $\xi = \pm 1$ and the diffusion error goes to infinity. Therefore, the time step is more likely to be cut at high absolute values of pitch. Using the Brownian bridge reduces the variance of the Wiener process increments. Therefore, not using the Brownian bridge results in a Wiener process with too much variance and, thus, the relative importance of the stochastic part in Eq. (88) becomes too great. Correspondingly, the importance of the deterministic part is too low. Since the deterministic part is always driving the pitch towards zero, one would expect that, when its value is to low with respect to the stochastic part, the pitch would be biased towards ± 1, which is exactly what happens in figure 7.b.

To verify the Milstein method and the Brownian bridge for the slowing-down of fusion alpha particles, an axisymmetric magnetic background for ITER baseline scenario was used. In these simulations, 1000 alphas were evenly distributed in volume and given a weight according to local fusion reaction rate: the greater the reaction rate, the greater the weight. These test particles were simulated until their temperature was two times the temperature of the background plasma. The simulations were run with the Milstein method and the Brownian bridge as well as with the Euler-Maryuama and fixed time-stepping. In both cases the slowing-down times of the particles were between 0.1 and 1.1 seconds. The differences in the slowing-down density distribution were within error bars, arising from the limited number of test particles (Fig. 8). This indicates that the adaptive time-stepping is valid for slowing-down simulations as well.

Simulation CPU-times between fixed and adaptive time-stepping were compared for helium and alphas to show the efficiency of the apadtive approach over the fixed one. The simulation time was set to 1 ms and the simulations were done in an axisymmetric magnetic background for ITER. The lowest and highest time steps

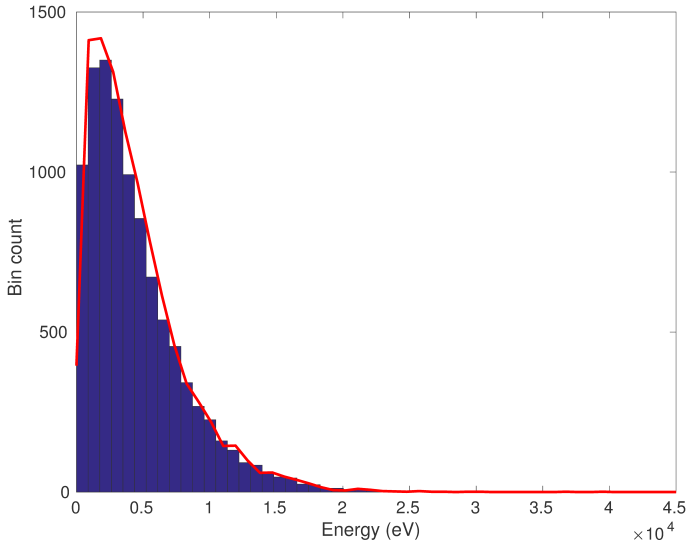

Figure 6: Final energy distribution of 10 000 thermal hydrogen particles with $T = 3$ keV (histogram) and a distribution of 10 000 data point, sampled straight from a Maxwellian distribution (red curve).

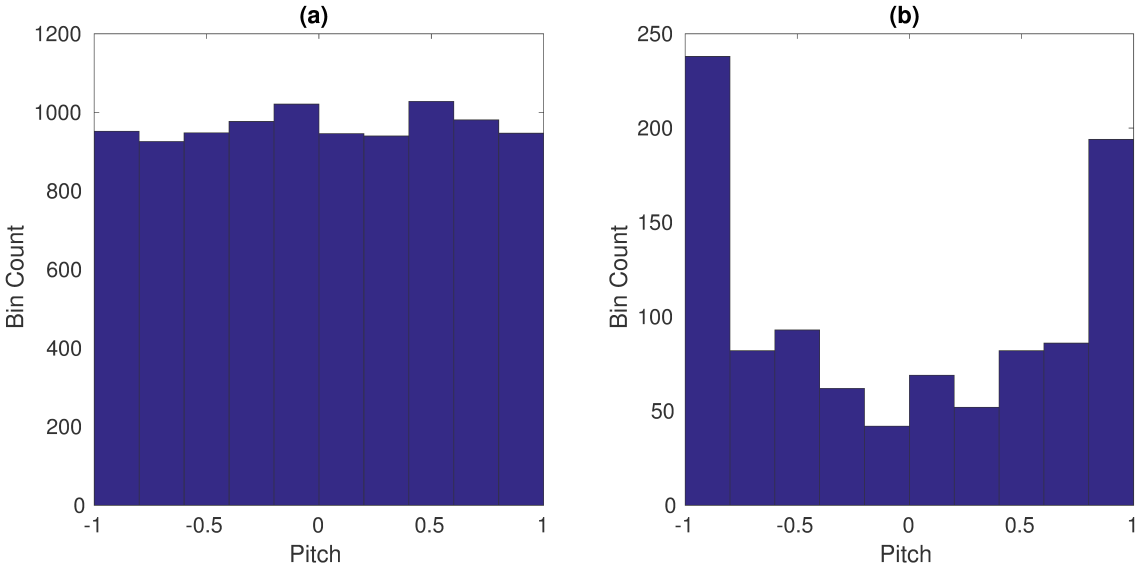

Figure 7: Final pitch distribution for thermal hydrogen ions (a) with and (b) without Brownian bridge. For the "with case" ten thousand ions were simulated. For the "without case" thousand ions were used since this was sufficient to bring up the faulty behavior.

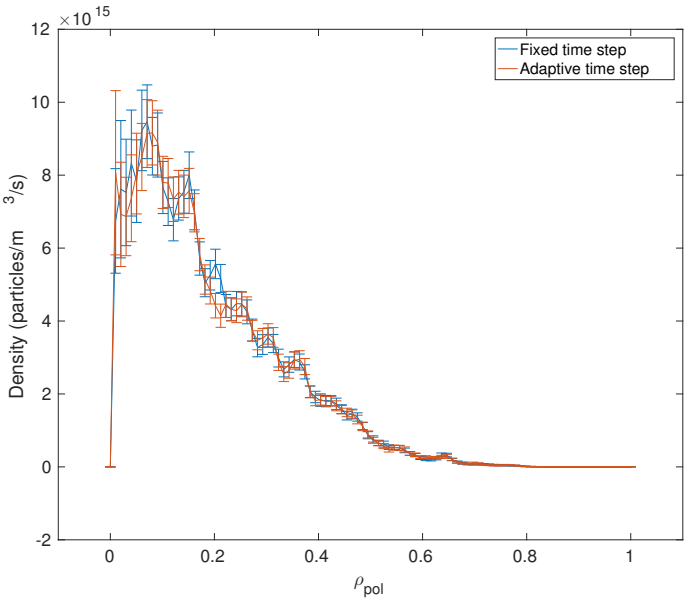

Figure 8: The spatial slowing-down density distribution with fixed and adaptive time stepping. The error bar width is one standard deviation. As more particles were initiated at high values of ρ_{pol} (due to these higher ρ_{pol} values encompassing larger volumes) with lower weights (due to lower fusion reaction rate), the distribution in the core is defined by few test particles with heavy weights, making the error bars larger. The small oscillations in the distribution are due to the effect of finite orbit-width of the alphas combined with too few particles to average these differences out.

Table 2: Comparison of maximal and minimal time steps with the Milstein method between different Milstein error tolerances for helium ash and alpha particles. The CPU-times between the adaptive Milstein method and the Euler-Maryuama method with fixed time step are also compared. The time steps for fixed time-stepping are chosen to be the smallest time steps from adaptive time-stepping.

	Δt_{min}	Δt_{max}	Milstein (low tolerance)	Euler (small Δt)
Helium	9e-12 s	4.20e-8 s	9.42 s	2.95e3 s
Alphas	4e-12 s	2.19e-5 s	95 s	6.58e3 s

	Δt_{min}	Δt_{max}	Milstein (high tolerance)	Euler (large Δt)
Helium	9.58e-8 s	1.50e-6 s	0.015 s	0.29 s
Alphas	3.21e-10 s	3.36e-4 s	0.45 s	82.5 s

from these simulations with adaptive time-stepping are listed in Table 2. The lowest steps were used to reproduce the simulations with the Euler-Maruyama method and fixed time step to make the comparison of the performance of the two methods. The difference between the highest and lowest time steps indicates that the adaptive time stepping scheme should reduce the computational time compared to the fixed time step scheme. In table 2, high tolerance for the Milstein method means 10^{-4} (see section 4.3). For low tolerance, the ratio was 10^{-5}.

5 Helium Ash Simulations in ITER Baseline Scenario with ELM Control Coils

The effect of the MPs is two-fold: they create regions of magnetic islands in the plasma and make the magnetic field on the edge stochastic. The stochasticity of the field lines facilitates the loss of particles from the confinement. The magnetic islands, on the other hand, could act as transport barriers. The transport barrier effect would both lead to better confinement and prevent re-entry. The re-entry of helium ash was simulated for this thesis in ITER, and compared to the results of Schmitz et al. [19] (recall section 2.2).

For the helium ash simulations, magnetic backgrounds from fast ion confinement studies with ASCOT were used [36]. In addition to the MPs due to ECCs, the backgrounds contain also other importaint, non-axisymmetric perturbations to the magnetic fields. These included ferritic inserts (FIs) that mitigate the toroidal field ripple arising from the finite number (18) of toroidal field coils, and test blanket modules (TBMs) that are used for breeding tritium from lithium [21]. Some of the FIs contributing to the background are also modified to allow the inclusion of neutral beam injectors that are used to heat the plasma. The magnetic fields were produced by combining the field from the magnetisation of ferromagnetic components (FIs and TBMs) to the field resulting from the poloidal and toroidal field coils and the plasma current. The magnetisation was obtained using finite element method with COMSOL [37] and the magnetising field itself using the Biot-Savart law integrator BioSaw [38]. The fast ions studied with these backgrounds included 3.5 MeV alpha particles and 1 MeV NBI deuterons. The aim was to examine the effect of TBMs (and MPs) on the wall power loads from these ions [21].

From the fast ion results reported in [36] and [21], it was concluded that the particles are overall well confined, if MPs are not present, but the losses that do occur peak at two energy regimes. The energy spectrum of the alpha particle losses with different magnetic perturbations (Fig. 3) is such that the losses are highest at high energies, due to prompt losses of particles which initially follow the stochastic field lines at the. The losses increase again as the alpha particles cool down towards helium ash. These losses are due to neoclassical transport, which is slow enough to let the alphas cool to helium ash before they are lost. Such loss spectrum is beneficial from the point of view of helium removal. However, the losses increase significantly overall when the MPs are included due to radial widening of the region with stochastic field lines. Also, the proportion of the losses at the lower end of the energy spectrum decrease with MPs. Losses at energies lower than 0.35 MeV consist of over 30% of the total particle losses with only FIs and TBMs present, but the inclusion of MPs reduces this share to around 14%. Therefore, even though the helium ash losses are increased by the MPs, this happens at the cost of alpha losses increasing even more. Similar energy loss spectra, as the ones obtained with ASCOT, have been predicted for DEMO [39].

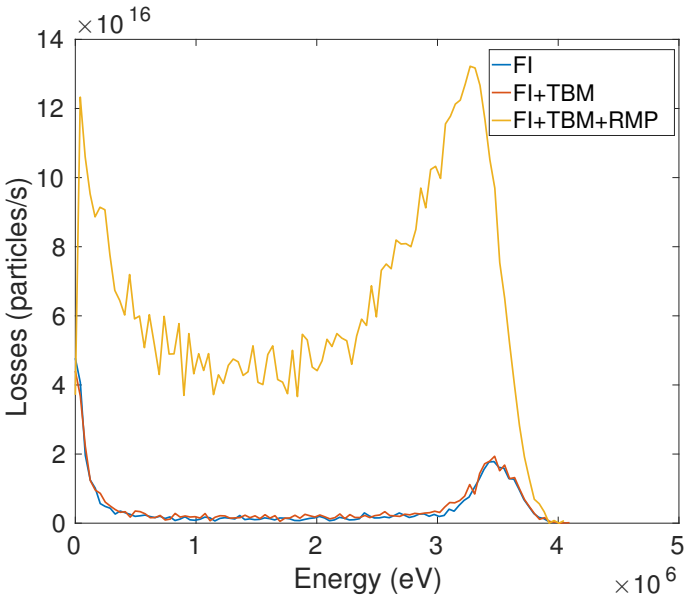

Figure 9: Alpha losses in ITER 15 MA scenario as a function of energy with FIs, TBMs and MPs. Most losses occur either as prompt losses or at low energies. Data from the RIPLOS2 project [21].

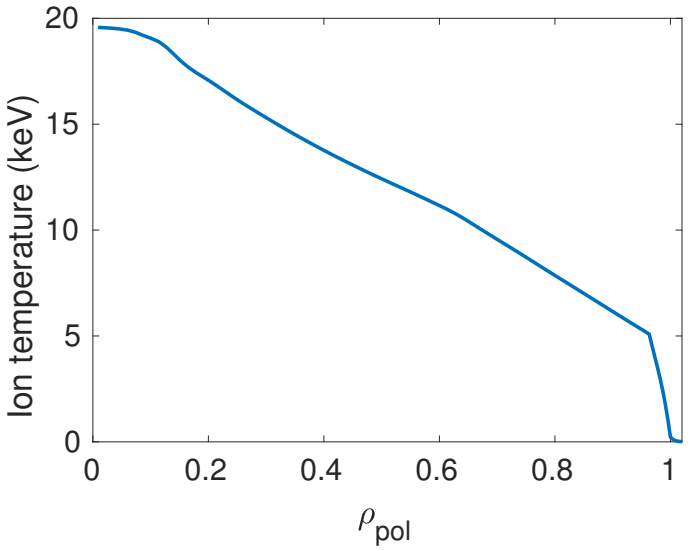

Figure 10: Ion temperature distribution in ρ_{pol} of ITER plasma for the baseline scenario. Data from the RIPLOS2 project [21].

The helium ash simulations were run for the baseline scenario and two regions of the plasma were considered: just outside the $q = 1$ surface (at $\rho_{pol} \approx 0.53$), where sawtooth takes place, and at the edge of the plasma, where the magnetic background is stochastic in the presence of MPs (recall Fig. 3). In both regions, magnetic islands are present but in general the magnetic field is smooth in the central region and stochastic at the edge. The simulations were run in two magnetic background configurations: the first one containing FIs and TBMs, and the second

one containing FIs, TBMs and MPs. In this way, any differences on the magnetic field between the two backgrounds were due to MPs only. In these simulations, 1000 particles were initially uniformly distributed in ϕ_{tor} and at different locations in ρ_{pol}: at ten equispaced ρ_{pol}-surfaces from $\rho_{pol} = 0.55$ to $\rho_{pol} = 0.6$ in the proximity of the $q = 1$ surface and at $\rho_{pol} = 0.9$ and $\rho_{pol} = 0.95$ at the edge. The simulations ran for 1 ms around $q = 1$ and 10 ms at the edge, which, in both cases, is longer than the collision time of thermal particles at the used background temperature (recall Fig. 5). The test particles were given energy corresponding to the temperature of the background plasma (Fig. 10).

It should be noted that ASCOT is designed for the simulation of minority plasma species, *i.e.* species that are so few in numbers in the plasma that they are not considered to be colliding with each other or affecting the background plasma profiles. In ITER, even though its fraction is to be kept under 10%, helium is no longer a minority species.

5.1 Simulation Results at $q = 1$ Surface

The region close to the $q = 1$ surface was chosen as a simulation location, because it has both magnetic islands and closed ρ_{pol}-surfaces outside them. This region is compared to the edge region, where the field lines outside the magnetic islands are stochastic.

The magnetic islands around the $q = 1$ surface increased the inward radial spread of the helium (Fig. 11). The enhanced inward spread was more pronounced in the presence of the ECCs due to the islands being wider in ρ_{pol} in this background. The enhanced inward spread was due to some of the particles initially residing inside the magnetic islands: since the particles follow field lines, and inside islands the field lines span a greater section of ρ_{pol}, the islands result in increased transport in ρ_{pol}. To examine the effect of the field without the islands the particles launched initially inside them were removed. In this case, the spread was roughly even inwards and outwards. Furthermore, without the islands, there was no significant difference whether the ECCs were used or not. It should be noted that, even though the magnetic islands actually increased radial spread of helium in this set of simulations, none of the simulated particles could penetrate past the island region. The spread in question is not radial transport but helium following the circular magnetic field lines inside magnetic islands.

5.2 Simulation Results at the Edge

According to ASCOT simulations, the use of MPs increased helium transport and losses. The increased transport can be seen from widening of the final ρ_{pol} distributions when the ECCs are turned on. This is true for test particles launched at $\rho_{pol} = 0.9$ (Fig. 12.c and 12.d) as well as for test particles launched at $\rho_{pol} = 0.95$ (Fig. 12.e and 12.f). The losses can be identified as a peak in the ρ_{pol}-distribution for $\rho_{pol} > 1$ in Fig. 12.f: the wall and the divertor reside in this radial location. When a particle impacts the wall or the divertor, the simulation for that particle

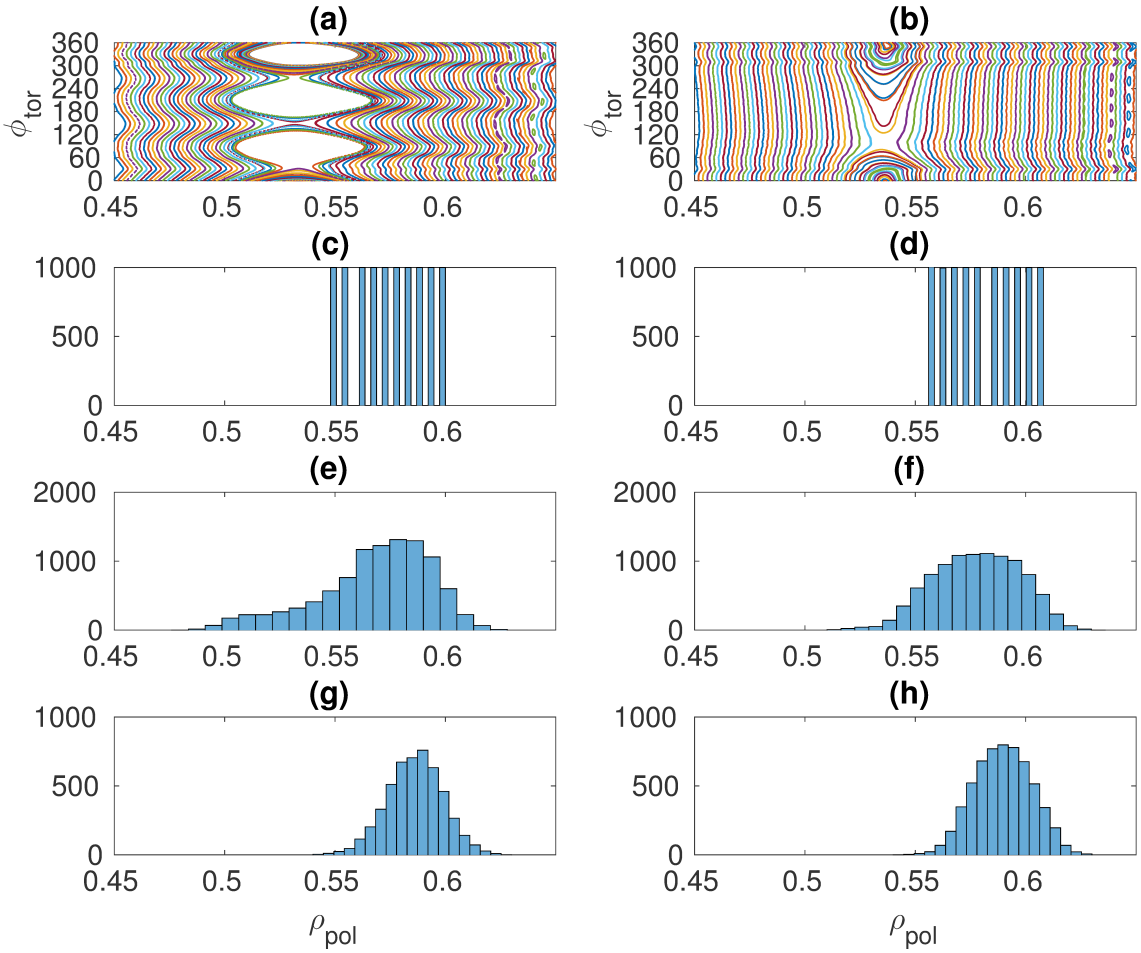

Figure 11: Radial evolution of helium ash around $q = 1$ surface (at $\rho_{pol} \approx 0.53$). Upper row shows Poincaré plots for the ITER baseline scenario in (a) with and (b) without ECCs. The left column contains result in the presence of ECCs, the right column without them. (c) and (d) show the initial locations of particles in ρ_{pol}, (e) and (f) their final locations, and (g) and (h) the final locations of particles with initial $\rho_{pol} > 0.575$, *i.e.* outside the magnetic islands.

is terminated resulting in the observed peak. A similar peak is not visible in Fig. 12.e, indicating larger losses when using ECCs.

The magnetic islands were predicted to act as weak transport barriers for the helium: the helium spread farther inside, relative to their inital position, if the particles were initiated at $\rho_{pol} = 0.95$ than when initiated at $\rho_{pol} = 0.9$. In the latter case, more islands were present immediately inside from the initial location. The distribution of final ρ_{pol} had its mean at 0.9 but had a positive skewness [40] of 0.22, indicating a more effective outward than inward diffusion. However, the skewness of 0.22 is low, and Fig. 12 can be observed to be quite symmetric. The effect of individual island regions can also be identified. ρ_{pol} values at the boundaries of island regions correspond to step-like falls in the number of particles penetrating further inwards at $\rho_{pol} = 0.9$, $\rho_{pol} = 0.87$ and $\rho_{pol} = 0.86$. This effect was more pronounced without MPs, as seen from local minima in the particle numbers at $\rho_{pol} = 0.89$ and $\rho_{pol} = 0.875$, where there are island boundaries. This could be because the islands' transport barrier effect is more effective the more thoroughly the islands span ϕ_{tor}, *i.e.* when the islands in the same radial location do not have stochastic regions between them as is the case for some islands when using ECCs. Another explanation is that the falls are not that prominent in the presence of ECCs, because MPs and other 3D-perturbations twist the ρ_{pol}-surfaces (Fig. 12.a and 12.b), and this twist has not been taken into account, *i.e.* ρ_{pol} is assumed axisymmetric.

To test the idea that thorough spanning of ϕ_{tor} improves the barrier properties of the islands, two more delta spikes, initiated at $\rho_{pol} = 0.91$ and $\rho_{pol} = 0.866$, were simulated. For these two new cases, the islands manifested themselves more as spikes in the final ρ_{pol} deposition than the step-like structure (Fig. 13). Inside from $\rho_{pol} = 0.866$, the islands effectively cover all toroidal angles and were expected to form a very effective transport barrier. Indeed, the islands inside from $\rho_{pol} = 0.866$ turned out to be an effective transport barrier as expected (Fig. 13.a). However, so did the islands outside from the location in question, even though these islands had stochastic regions between them, and, overall, the distribution of final ρ_{pol} in this case was not skewed (with mean 0.866 and skewness -0.01). This can also be seen from Figs. 14.a and 14.b: 38%-39% of the particles that were transported to $\rho_{pol} = 0.866 \pm 0.02$. Inside from $\rho_{pol} = 0.91$, the islands span about half of the toroidal angles at $\rho_{pol} = 0.9$, whereas only a fourth at $\rho_{pol} = 0.92$, outside from the initial location. The particles initially at $\rho_{pol} = 0.91$ diffused more effectively outwards than inwards (skewness 0.38). In fact, even the mean of the distribution shifted slightly from the initial location to $\rho_{pol} = 0.913$, indicating an outward transport. However, the effect of the first island regions both in- and outwards did not seem to be important: 50%-51% of the outward moving particles reached $\rho_{pol} = 0.925 \pm 0.015$. These ρ_{pol}-surfaces mark roughly the outer ends of the first regions of magnetic islands the particles reach.

The barrier property of the islands was also compared between helium and deuterium by simulating also 1000 deuterium ions launched from $\rho_{pol} = 0.9$ and $\rho_{pol} = 0.95$. The use of ECCs caused more losses on deuterium (Fig. 16) than on helium. Since the stochastic field lines eventually take the particles following them to the wall, the deuterium reaches the wall faster as it has lighter mass but

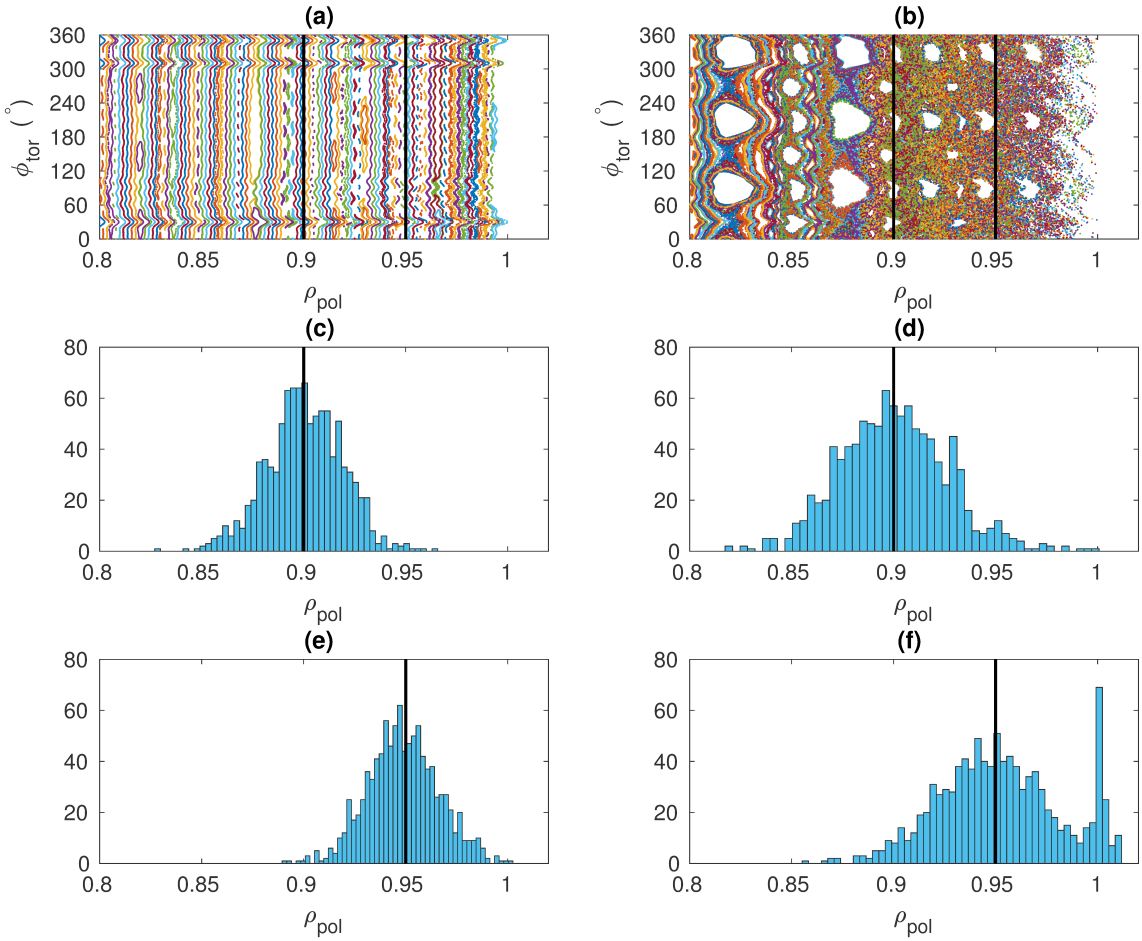

Figure 12: Radial evolution of helium ash at the edge of the plasma. Upper row shows Poincaré plots for the ITER baseline scenario in (a) without and (b) with ECCs. The left column contains results in the presence of ECCs, the right column without them. (c) and (d) show the final locations of particles initiated at $\rho_{pol} = 0.9$, and (g) and (h) the final locations of particles initiated at $\rho_{pol} = 0.95$. The black lines denote the inital radial locations of the particles.

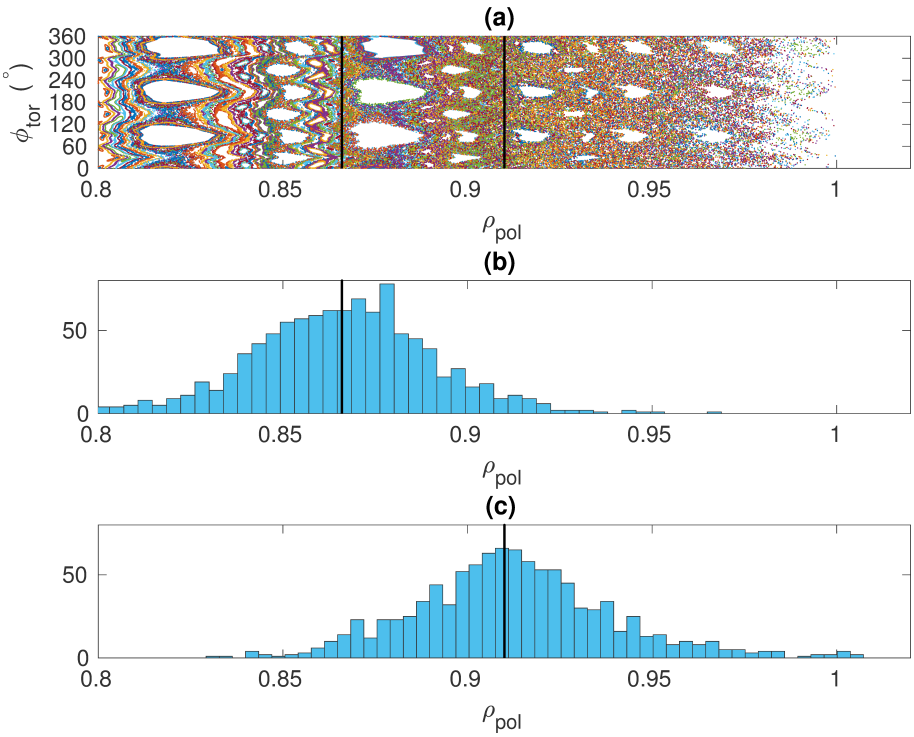

Figure 13: (a) Poincaré plot of the edge in the ITER baseline scenario with ECCs and the final radial locations of helium particles initiated at $\rho_{pol} = 0.866$ (b) and $\rho_{pol} = 0.91$ (c) in the presence of MPs. The black lines denote the inital radial locations of the particles.

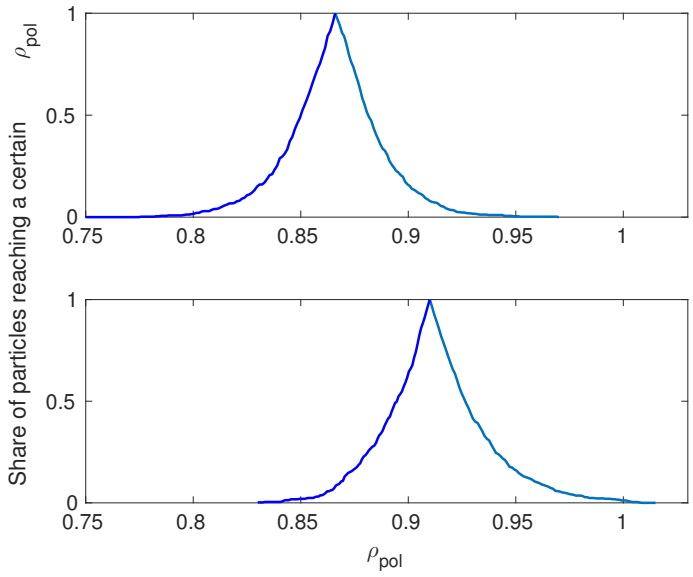

Figure 14: Share of inward and outward moving particles starting from (a) $\rho_{pol} = 0.866$ and (b) $\rho_{pol} = 0.91$ reaching a certain ρ_{pol}. The Inside curve (dark blue) in each figure presents the inward moving particles and the right curve (light blue) the outward moving ones.

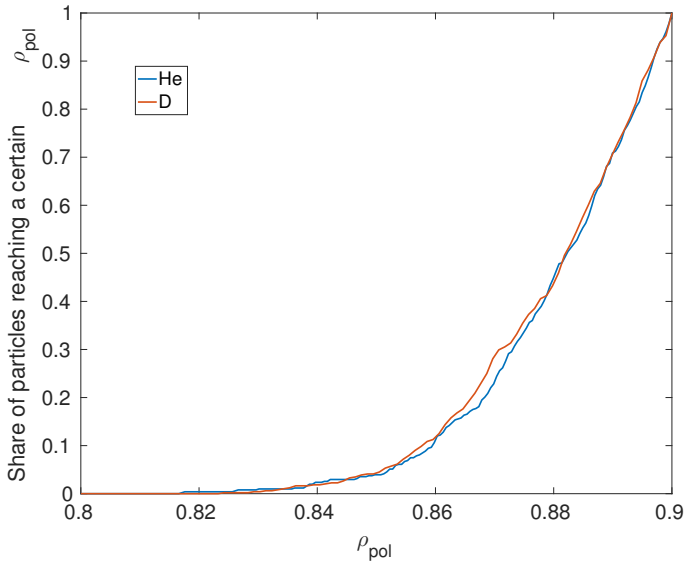

Figure 15: Share of inward moving particles starting from $\rho_{pol} = 0.9$ reaching a certain ρ_{pol}.

similar energy compared to the helium, resulting in higher velocity. The outward diffusion was stronger for deuterium, than it was for helium, when particles were initiated at $\rho_{pol} = 0.9$. In this case, the mean of the distribution of final ρ_{pol} was still at 0.9 but the skewness was 0.37 (compared to 0.22 for helium). The island manifested themselves, again, with a more spike- than step-like structures in the distributions of final ρ_{pol}. The effect of the islands did not differ much between deuterium and helium: the inward diffusion was about similar for both species (Fig. 15). Since the lighter mass of deuterium led to worse confinement compared to helium, one would expect a similar effect between deuterium, tritium and hydrogen. Due to its lighter mass, hydrogen should have a worse confinement than deuterium. Conversely, confinement of heavier tritium would be better than that of deuterium, leading to fuel segregation.

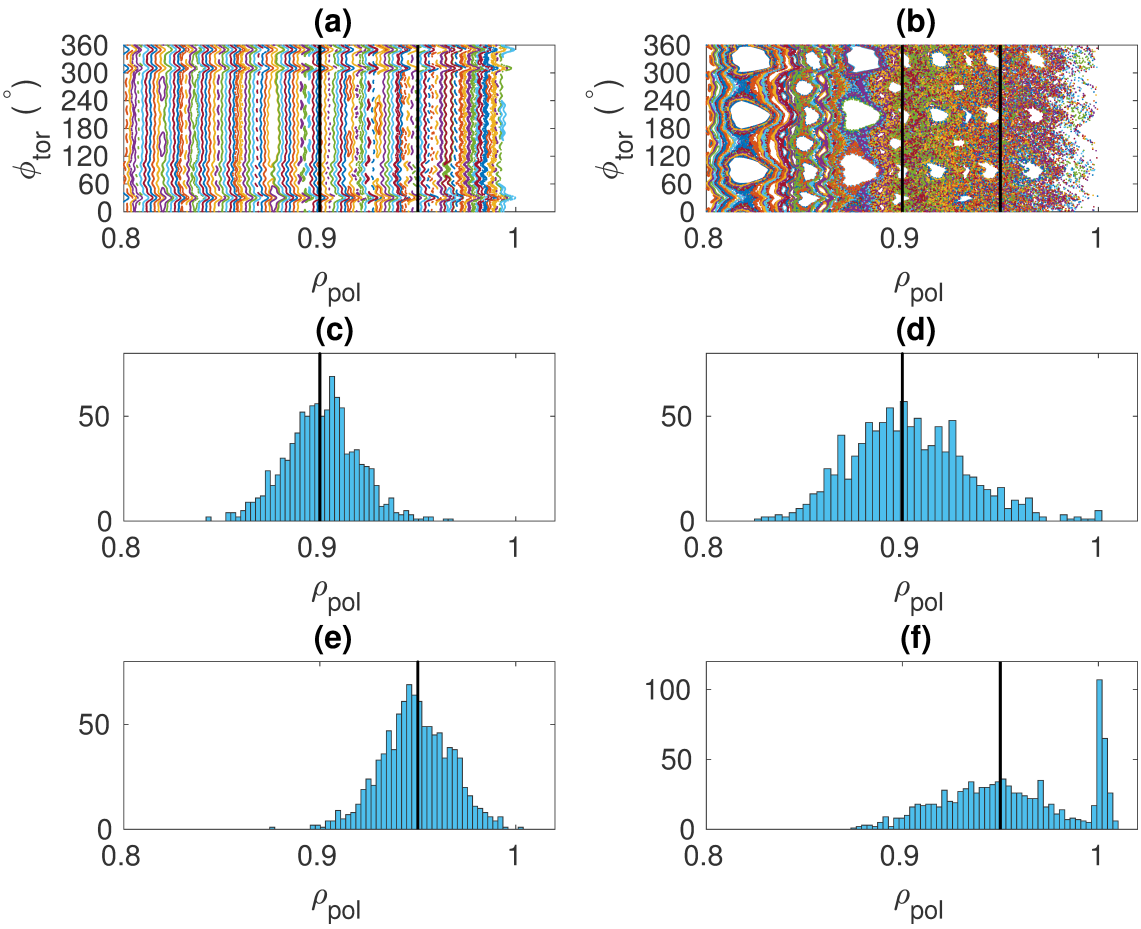

Figure 16: Poincaré plot of the edge in the ITER baseline scenario (a) without ECCs and (b) with them and the final radial locations of deuterium particles (c) without MPs initiated at $\rho_{pol} = 0.9$, (d) with ECCs initiated at $\rho_{pol} = 0.9$, (e) without MPs initiated at $\rho_{pol} = 0.95$, and (f) with ECCs initiated at $\rho_{pol} = 0.95$ (Note that the upper limit of the y-axis is different from the other plots). The black lines denote the inital radial locations of the particles.

6 Summary and Discussion

In this thesis, simulations with orbit-following Monte Carlo code ASCOT were carried out to assess helium re-entry in ITER by using MPs erected by ECCs. ASCOT's numerical toolkit had to be upgraded to carry out simulations of thermal particles, such as the helium ash. These improvements included implementation of the Milstein method for numerically integrating ASCOT's collision operator, which guarantees convergence of paths of individual particle paths to the exact solution as the integration time step is reduced. Another improvement was made by adaptive time-stepping with a Brownian bridge. The Brownian bridge guarantees correct generation of Wiener processes for SDEs and adaptive time-stepping speeds up the simulations.

Three methods to mitigate helium ash accumulation were introduced: the MP-method studied in this thesis, the use of sawtooth oscillations to remove helium from core plasma, and the use of ICRH to transport helium to the edge of the plasma. The MP-method was chosen as a first application for the Milstein method in ASCOT.

In the simulations it was found that the magnetic islands acted as transport barrier in stochastic background magnetic field. However, the effectiveness of the barriers looks limited, and the outward transport of deuterium in the perturbed magnetic field was greater than the outward transport of helium. Therefore, using a stochastic field structure with islands to enhance helium removal requires that the bulk plasma is effectively kept out of this region of the magnetic field. The enhanced outward transport of lighter ions could also lead to fuel segregation due to lighter mass of deuterium compared to tritium. A second concern is that the effect of the 3D-perturbations in the simulations was greater on alphas than on helium. Overall, the use of magnetic islands as helium transport barriers is not predicted to be very efficient in ITER.

These studies indicate some limitations in the performed ASCOT simulations. These can be divided in two categories: limitations due to input parameters and more global limitations in ASCOT. First, the magnetic fields including MPs were optimized for ELM-mitigation and not for blocking inward transport of helium. Secondly, the plasma response, which would shield the plasma from the effect of the perturbation, was not taken into account. If suitable fields were available, both of these could be taken into account in future simulations to draw more definite conclusions about the usefulness of magnetic islands for preventing helium re-entry.

To consider more general limitations, ASCOT simulations do not take into account the impact of plasma turbulence on helium transport. Fortunately, the transition from L-mode to H-mode eliminates the turbulence at the edge. Around $q = 1$, on the other hand, sawtooth oscillations have an impact on the helium transport, which is not taken into account. Another general point is that the simulations did not include effects of the radial electric field, since its form is not known in a stochastic magnetic field.

Further ASCOT studies with helium ash could be done, when the code is upgraded to simulate ICRH heated particles. If the inversion radius of the sawtooth crash does not reach the stochastic region, ICRH could enhance the outward trans-

port of helium there. With ICRH, ASCOT simulations coupling the ICRH and the effect of the MPs could be made to examine helium removal from the sawtooth inversion radius to outside the plasma.

References

[1] Fuelling the Fusion Reaction, https://www.iter.org/sci/FusionFuels, Referenced: 23.9.2016.

[2] Triple Product, https://www.euro-fusion.org/glossary/triple-product/, Referenced: 5.10.2016.

[3] Wesson, J. Tokamaks, 4. edition, *Oxford Science Publications*, 2011.

[4] Hirvijoki, E. et al. ASCOT: solving the kinetic equation of minority particle species in tokamak plasmas, *Computer Physics Communications*, **185**, 1310-1321, 2014.

[5] Miettunen, J. Modelling of Global Impurity Transport in Presence of Non-axisymmetric Effects, PhD thesis, Aalto University, 2015.

[6] Reiter D. et al. Burn Condition, helium Particle Confinement and Exhaust Efficiency, *Nuclear Fusion*, **30**, 10, 1990.

[7] Zastrow K.-D. et al. Helium exhaust experiments on JET with Type I ELMs in H-mode and with Type III ELMs in ITB discharges, *Nuclear Fusion*, **45**, 3, 2005.

[8] Garcia J. et al. Key impact of finite-beta and fast ions in core and edge tokamak regions for the transition to advanced scenarios, *Nuclear Fusion*, **55**, 053007, 2015.

[9] Wagner, F et al. Development of an Edge Transport Barrier at the H-Mode Transition of ASDEX, 1984 *Physical Review Letters* **53**, 1453.

[10] Zohm, H Edge Localized Modes (ELMs), 1996, *Plasma Phys. Control. Fusion* **38**, 105.

[11] Wolf R.C. Internal transport barriers in tokamak plasmas, *Plasma Physics and Controlled Fusion*, **45**, 1, 2002.

[12] Hogan J. Helium transport and exhaust experiments in tokamaks, *Journal of Nuclear Materials*, **241-243**, 68, 1997.

[13] Wade M.R. et al. Helium transport and exhaust studies in enhanced confinement regimes in DIIID, *Physics of Plasmas*, **2**, 2357, 1995.

[14] Sakasai A. et al. Helium exhaust in divertor-closure configuration with W-shaped divertor of JT-60U, *Journal of Nuclear Materials*, **290-293**, 957-961, 2001.

[15] Sakasai A. et al. Steady-State Exhaust of Helium Ash in th W-Shaped Divertor of JT-60U, *Proceedings of the 17th International Conference on Fusion Energy*, Yokohama, 1998.

[16] Chapman I. Controlling sawtooth oscillations in tokamak plasmas, *Plasma Physics and Controlled Fusion*, **53**, 1, 2010.

[17] Hamamatsu K. et al. Numerical Analysis of Helium Ash Removal by Using ICRH-Driven Ripple Transport, *Plasma Physics and Controlled Fusion*, **40**, 255-270, 1998. s

[18] Evans T. E. et al. Suppression of Large Edge-Localized Modes in High-Confinement DIII-D Plasmas with a Stochastic Magnetic Boundary, *Physical Reviw Letters*, **92**, 23, 2004.

[19] Schmitz O. et al. Enhancement of helium exhaust by resonant magnetic perturbation fields at LHD and TEXTOR, *Nuclear Fusion*, **56**, 10, 2016.

[20] Koskela, T. Monte Carlo simulation of fast ion losses in ITER in the presence of static 3D magnetic perturbations, PhD thesis, Aalto University, 2014.

[21] Kurki-Suonio, T. et al. Final Report for the project F4E-GRT-379, 'RIPLOS-2'.

[22] Øksendal, B. Stochastic Differential Equations - An Introduction With Applications, 6. Edition, *Springer-Verlag*, 2003.

[23] Glasserman, P. Monte Carlo Methods in Financial Engineering, 1. Edition, *Springer*, 2003.

[24] Kloeden, P.E., Platen E. Numerical Solution of Stochastic Differential Equations, 3. Edition, *Springer*, 1999.

[25] Gaines, J.G., Lyons T.J. Variable Step Size Control in the Numerical Solution of Stochastic Differential Equations, *SIAM Journal of Applied Mathematics*, **57**, 1455-1484, 1997.

[26] Lamba, H. An adaptive timestepping algorithm for stochastic differential equations, *Journal of Computational and Applied Mathematics*, **161**, 417-430, 2003.

[27] Cary, J. R., Brizard A. J. Hamiltonian theory of guiding-center motion *Reviews of Modern Physics*, **81**, 693, 2009.

[28] Ichimaru S. Statistical Plasma Physics, *Frontiers in Physics*, 1. Edition, 1992.

[29] Hirvijoki, E. et al. Monte Carlo Method and High Performance Computing for Solving Fokker-Planck Equation of Minority Plasma Particles, *J. Plasma Physics* **81**, 435810301, 2015.

[30] Koskinen H. Johdatus plasmafysiikkaan ja sen avaruussovelluksiin, *Limes ry*, 1. Edition, 2001.

[31] Hirvijoki, E. Theory and models for Monte Carlo simulations of minority particle populations in tokamak plasma, PhD thesis, Aalto University, 2014.

[32] Brizard A. J. et al. A Guiding-centre Fokker-Planck Collision Operator for Non-Uniform Magnetic Fields, *Physics of Plasmas*, **11**, 4429-4438, 1998.

[33] Hirvijoki E. et al. Monte Carlo Implementation of Guiding-Centre Fokker-Planck Kinetic Equation, *Physics of Plasma*, **20**, 9, 2013.

[34] Box, G. E. P., Muller, M. E. A Note on the Generation of Random Normal Deviates. *Ann. Math. Stat.* **29**, 610-611, 1958.

[35] *http://se.mathworks.com/help/stats/chi2gof.html*, Referenced: 2.8.2016.

[36] Varje, J. et al. Modelling of 3D fields due to ferritic inserts and test blanket modules in toroidal geometry at ITER, *Nuclear Fusion* **56**, 066001, 2016.

[37] Äkäslompolo S. et al. Calculating the 3D magnetic field of ITER for European TBM studies, *Fusion Engineering and Design*, **98-99**, 1039-1043, 2015.

[38] Äkäslompolo S. et al. "Biot Savart Law integrator BioSaw." arXiv preprint arXiv:1511.01629 (2015).

[39] Pfefferle D. et al. Effects of magnetic ripple on 3D equilibrium and alpha particle confinement in the European DEMO, *Nuclear Fusion*, **56**, 11, 2016.

[40] *https://se.mathworks.com/help/stats/skewness.html*, Referenced: 6.10.2016.